Rigorous Fit to the Peak Region of the Thrust Distribution

by

Jeffrey C. Prouty

Submitted to the Department of Physics
in partial fulfillment of the requirements for the degree of

Bachelor of Science in Physics

at the

MASSACHUSETTS INSTITUTE OF TECHNOLOGY

June 2014

Author ..... Signature redacted .....
Department of Physics
May 9, 2014

Certified by ..... Signature redacted .....
Iain Stewart
Professor, Department of Physics
Thesis Supervisor

Accepted by ..... Signature redacted .....
Professor Nergis Mavalvala
Senior Thesis Coordinator, Department of Physics

Rigorous Fit to the Peak Region of the Thrust Distribution

by

Jeffrey C. Prouty

Submitted to the Department of Physics
on May 9, 2014, in partial fulfillment of the
requirements for the degree of
Bachelor of Science in Physics

Abstract

We continue the work of Abbate et al. in [1], in which a factorization formula for the thrust distribution in electron-positron collisions was developed in the framework of soft-collinear effective theory. We extend the analysis of thrust to the peak region of the distribution, in which a nonperturbative soft function encoding the effects of large-angle soft gluon radiation plays a significant role. We write the soft function as an infinite sum of basis functions and use a truncated version in our calculations, allowing us to fit for the basis coefficients c_i with all available thrust data from center-of-mass energies $Q = 35$ to 207 GeV. To characterize the soft function independently of a particular parameterization, we present fit results for its cumulant moments, denoted Ω_i', up to $i = 4$. We compute experimental uncertainties from the fits and theory uncertainties using a random scan in the space of the undetermined parameters of the theory. Our approach significantly improves the fit in the peak region, reducing the minimum χ^2/d.o.f. value from to 5.29 using the best fit form the tail region without fitting basis functions, to 1.23 using five basis functions. We find $\Omega_1 = 0.387 \pm (0.003)_{\text{exp}} \pm (0.026)_{\text{pert}}$ GeV, indicating that the peak region determines Ω_1 with considerably more precision than the tail. For the second cumulant moment, we find $\Omega_2' = 0.032 \pm (0.002)_{\text{exp}} \pm (0.011)_{\text{pert}}$ GeV^2. We also estimate the third and fourth cumulant moments, obtaining $\Omega_3' = [3.5 \pm (0.7)_{\text{exp}} \pm (2.3)_{\text{pert}}] \times 10^{-3}$ GeV^3 and $\Omega_4' = [-0.7 \pm (3.8)_{\text{exp}} \pm (11.9)_{\text{pert}}] \times 10^{-4}$ GeV^4.

Thesis Supervisor: Iain Stewart
Title: Professor, Department of Physics

Acknowledgments

I sincerely thank my advisor, Iain Stewart, for his guidance, work and support on this project. I also thank Vicent Mateu and André Hoang for their contributions, without which this endeavor would not have been possible. I am also indebted to Jesse Thaler for connecting me to the group and providing support as my academic advisor. I thank the MIT UROP office for financially supporting me during the summer of 2012 and fall of 2013, enabling me to participate in this research. Finally, I would like to thank my family and friends at MIT, whose support has been unwavering and encouraging.

Contents

Chapter 1

Introduction

The production of hadrons in electron-positron annihilation provides one of the best methods for analyzing the predictions of both perturbative and nonperturbative quantum chromodynamics [3]. When an electron and a positron annihilate into a photon or Z boson, there is some probability of producing a quark-anitquark pair. Confinement ensures that when such an event occurs, the asymptotic states are hadrons. The process by which these hadrons form from the quarks and gluons produced during and immediately after the collision is called *hadronization.* The fluctuation of the boson into a quark-antiquark pair occurs on a timescale of $1/Q$, where Q is the center-of-mass energy of the collision, while hadronization occurs on a much larger timescale of $1/\Lambda_{\mathrm{QCD}}$, where Λ_{QCD} is the energy at which the running coupling α_s becomes large enough for perturbation series to diverge. As such, the physics of hadronization may be considered separately from pair-production for sufficiently high Q.

Hadrons produced in e^+e^- collisions have a rich jet structure dictated by QCD. Measurements of the jet structure provide us with a means of studying how the final state hadrons are kinematically distributed [4]. One approach to studying the jet structure of the final-state hadrons is to define an *event shape variable*, a function characterizing the distribution of hadrons in a particular event. Several recent achievements have significantly improved the theoretical descriptions of these event shape variables. In the work of Gehrmann et al. in Refs. [24, 25] and of Weinzierl in Refs. [26, 27], the $\mathcal{O}(\alpha_s^3)$ contributions to the 2-, 3- and 4-jet final states were deter-

mined. Additionally, soft-collinear effective theory (SCET) [28, 29, 30, 31] provides a systematic framework in which to treat nonperturbative corrections [33, 34] and compute at all orders in α_s the hard, collinear, and soft contributions to jet production [35, 36, 37]. SCET builds on earlier QCD all-order factorization results from Refs. [38, 39, 40].

In this thesis we are concerned with the variable *thrust*, most commonly defined by

$$T = \max_{\hat{t}} \frac{\sum_i |\hat{t} \cdot \vec{p}_i|}{\sum_i |\vec{p}_i|}, \tag{1.1}$$

where $\vec{p}_i$ are the momenta of the final-state hadrons. In [1], Abbate et. al developed a factorization formula for the thrust differential cross section from e^+e^- collisions in the SCET framework. They performed a precision global fit for α_s in the so-called tail region of the distribution, defined below. The purpose of this work is to extend this analysis to another region, which we call the peak, in which uniform soft radiation has a significant impact on the cross section (note that whenever we refer to the cross section, we mean the differential cross section with respect to thrust). Following [1] we work with the alternative variable $\tau = 1 - T$, which we still call thrust, so that the range of τ is $[0, 0.5]$. Low values of thrust under this definition are associated with pencil-like two-jet events, each of which carry half of the total momentum in opposite directions. Higher values are associated with more jets, with the momenta of the hadrons more evenly distributed in space. For $\tau < 1/3$, the physics is governed by three different energy scales. The *hard scale* is defined by $\mu_H \approx Q$, the center-of-mass energy of the collision. The *jet scale* is given by $\mu_J \approx Q\sqrt{\tau}$ and is determined by the typical momentum transverse to $\hat{\mathbf{t}}$, the direction of greatest net momentum in each hemisphere. The *soft scale* characterizes the energy of uniform soft gluon radiation, with $\mu_S \approx Q\tau$.

The thrust distribution may be divided into three regions, in which different physical effects play the dominant role. In the *peak* region $\tau \sim 2\Lambda_{\mathrm{QCD}}/Q$, so that the hard, jet, and soft scales are approximately Q, $\sqrt{\Lambda_{\mathrm{QCD}} Q}$, and Λ_{QCD}, respectively. In this

region $\frac{d\sigma}{d\tau}$ has a strongly peaked maximum. Since $\mu_S \gtrsim \Lambda_{\rm QCD}$, hadronization effects play an important role. In the SCET framework this statement implies that the differential cross section is affected at leading order by a nonperturbative distribution, which we call the nonperturbative soft function, denoted $S_\tau^{\rm mod}$. In the *tail* region, associated with three-jet and broader two-jet events, the soft scale becomes much larger than $\Lambda_{\rm QCD}$, and so the soft radiation can be included plus a series of power corrections using perturbation theory. Finally, in the *far-tail* region the distinction of scales no longer has meaning, and accurate predictions can be made using only perturbation theory with power corrections.

The analysis in [1] by Abbate et al. has provided a high-precision determination of $\alpha_s(m_Z)$ by fitting to the tail region of the thrust distribution. The purpose of this thesis is to characterize the distribution in the peak region. The peak region is sensitive enough to the soft function that its higher moments become significant and must be fit to the experimental data. We denote the i-th moment of the model function by Ω_i. These moments are renormalization scheme-dependent, and details regarding their definition is given in Section 2.3. In the tail-region fits only the first moment of the distribution, Ω_1, plays a significant role, and so the fits in [1] were performed in (α_s, Ω_1) space. In the peak region we find that available e^+e^- collision data determines Ω_1 with considerably more precision. By also fitting moments Ω_2, Ω_3, and Ω_4, we obtain a significantly improved description of the experimental data. This fit to higher moments is achieved by writing the nonperturbative soft function as a sum of orthogonal basis functions, developed by Ligeti et al. in [9], and treating the coefficients of these basis functions c_i as our fit parameters.

The factorization formula developed by Abbate et al. is as follows:

$$\begin{aligned}\frac{d\sigma}{d\tau} = &\int dk \left(\frac{d\hat{\sigma}_{\rm s}}{d\tau} + \frac{d\hat{\sigma}_{\rm ns}}{d\tau} + \frac{\Delta d\hat{\sigma}_b}{d\tau}\right)\left(\tau - \frac{k}{Q}\right) \times S^\tau_{\rm mod}\left(k - 2\bar{\Delta}(R,\mu_S)\right) \\ &+ \mathcal{O}\left(\sigma_0 \alpha_s \frac{\Lambda_{\rm QCD}}{Q}\right).\end{aligned} \tag{1.2}$$

We explain its perturbative components, $\hat{\sigma}_{\rm s}$, $\hat{\sigma}_{\rm ns}$, and $\hat{\sigma}_{\rm b}$ in Chapter 2 and its nonper-

turbative component $S^{\tau}_{\rm mod}$ in Chapter 3. We focus on the aspects of the factorization formula which are particularly relevant for fits in the peak region and direct the reader to [1] for more detail. In Chapter 4 we present our analysis of the peak region and the results of our fits for moments of the soft function, including both experimental and theoretical uncertainties. In Chapter 5 we present our conclusions and plans for work in the future.

Chapter 2

Perturbative Components

2.1 Singular and Nonsingular Distribution

The perturbative components of the differential cross section in Eq. (1.2) are contained in a singular piece $\frac{d\hat{\sigma}_s}{d\tau}$, a nonsingular piece $\frac{d\hat{\sigma}_{ns}}{d\tau}$, and a term $\frac{\Delta d\hat{\sigma}_b}{d\tau}$, which incorporates the effects of the mass of the bottom quark. The nonperturbative physics is encoded in the soft function $S^\tau_{\rm mod}$. Here our main concern is to determine the soft function in order to determine the nonperturbative physics involved in e^+e^- collisions. As such, we give only a brief overview of the perturbative terms. Included in this overview are the undetermined parameters of the theory relevant to fits in the peak region, which are significant for our estimates of the theory uncertainty in the moments of the soft function.

The contribution of singular terms in perturbation theory to the cross section (assuming massless quarks) is given by

$$\frac{d\hat{\sigma}_s^{\rm QCD}}{d\tau} = Q\sum_I \sigma_0^I H_Q^I(Q,\mu_H) U_H(Q,\mu_H,\mu)\int ds\, ds' J_\tau(s',\mu_J) U_J^\tau(s-s',\mu,\mu_J) \times \int dk'\, U_S^\tau(k',\mu,\mu_S) e^{-2\frac{\delta(R,\mu_S)}{Q}\frac{\partial}{\partial\tau}} S_\tau^{\rm part}\left(Q\tau - \frac{s}{Q} - k', \mu_S\right). \tag{2.1}$$

This singular partonic distribution contains terms $\propto \alpha_s^j \ln^k(\tau)/\tau$ and $\alpha_s^j\delta(\tau)$ from

perturbation theory. Here σ_0^I is the total hadronic cross section for quark production given a current type I, and we have a hard function H_Q^I, a jet function J_τ, and a partonic soft function S_τ^{part}. The U coefficients are renormalization group factors for summing large logarithms at different energy scales. There are four different renormalization scales at play in this formula: a hard scale μ_H, a jet scale μ_J, a soft scale μ_S, and a subtraction scale R. In general, their values need to be τ-dependent in order to sum logarithms and properly treat different regions, and so we use *profile functions* to describe their τ dependence [1, 9]. The profile functions are discussed in the next section.

Terms in the expansions of J_τ and S_τ^{part} are known up to N^{3}LL$'$ order and $\mathcal{O}(\alpha_s^3)$, and we use all of them in our highest order analysis. The order N^{3}LL is defined by terms of the form $\alpha_s^2 \sum_{k=0}^{\infty} (\alpha_s \log(\tau))^k$ that contribute to $\log\left(\sum_s(\tau)\right)$, where $\log\left(\sum_s(\tau)\right)$ is defined by $\sum_s(\tau) = \frac{1}{\sigma_0} \int_0^\tau \mathrm{d}\tau' \frac{\mathrm{d}\sigma_s}{\mathrm{d}\tau'}$. The prime denotes the inclusion of $\mathcal{O}(\alpha_s^3)$ terms not proportional to logarithms of τ. There are three undetermined parameters, however, which contribute to our theory uncertainty. The first, j_3, is an unknown coefficient of a non-logarithmic term that appears in the jet function at $\mathcal{O}(\alpha_s^3)$. We set it to zero by default and allow it to vary from -3000 to 3000 in our uncertainty estimate. This range, and those of the two parameters that follow, are derived from Padé approximation; see [1] for more detail. The second, s_3, is an unknown coefficient of another non-logarithmic term at $\mathcal{O}(\alpha_s^3)$, this time appearing in the partonic soft function. We also set it to zero by default and allow it to vary from -500 to 500. Finally, the $\mathcal{O}(\alpha_s^4)$ cusp anomalous dimension Γ_3^{cusp} is necessary to determine the renormalization group factor U_H, U_J, and U_S at N^{3}LL and N^{3}LL$'$. This parameter is unknown, but can be approximated from the known lower coefficients using a Padé approximant. We thus take its central value to be 1553.06 and allow it to vary by $\pm 200\%$ in our theory uncertainty estimation.

The nonsingular terms in perturbation theory are incorporated into the factorization in the nonsingular distribution given by

$$\frac{\mathrm{d}\hat{\sigma}_{\mathrm{ns}}}{\mathrm{d}\tau} = Q \sum_I \sigma_0^I e^{-2\frac{\delta(R,\mu_S)}{Q}\frac{\partial}{\partial\tau}} f^I\left(\tau, \frac{\mu_{\mathrm{ns}}}{Q}\right). \tag{2.2}$$

The superscript I denotes different currents just as in Eq. (2.1). The functions f_I are fixed-order partonic distributions determined in pure QCD with massless quarks. Modifications are possible to incorporate QED and bottom quark mass effects; in our peak analysis, we currently incorporate only QED effects. The $\mathcal{O}(\alpha_s)$ partonic thrust distribution is known analytically [5], and the $\mathcal{O}(\alpha_s^2)$ and $\mathcal{O}(\alpha_s^3)$ contributions are available numerically in FORTRAN and incorporated into our calculations (respectively, see [6, 7] and [8]).

In order to incorporate numerical uncertainties in the $\mathcal{O}(\alpha_s^2)$ and $\mathcal{O}(\alpha_s^3)$ distributions, our code makes use of two parameters, labelled ϵ_2 and ϵ_3. Setting these parameters to ± 1 corresponds to changing their associated distributions by $\pm 1\sigma$. We take both to be zero by default and vary both by ± 1 in our theory uncertainty analysis. It should be noted that the third order distribution and its error function also depend on the unknown coefficients s_3 and j_3, and our analysis accounts for this variation as well.

2.2 Profile Functions

Five different scales play a role in the factorization formula: μ_H, μ_J, μ_S, μ_{ns}, and R. For the singular partonic distribution $\frac{\mathrm{d}\hat{\sigma}_s}{\mathrm{d}\tau}$, there are three: a hard scale μ_H, a soft scale μ_S, and a jet scale μ_J, corresponding to the energy scales described in Chapter 1. A single value cannot be chosen for each of these scales μ_i and applied to all values of τ, because for μ_S and μ_J the scales must vary in different regions of the distribution such that large logarithms are summed in the peak and tail, but not in the far-tail region. The results for the μ_i are fixed in each region, but there is freedom for how to connect them between reasons. We use τ-dependent *profile functions* to determine the scales, allowing smooth transitions between the regions. We design these functions to be piecewise but continuous and smooth, such that the

first derivative is also continuous. Here we concern ourselves with their properties in the peak region.

Although the factorization formula is formally invariant under changes in the profile functions which do not modify the hierarchy [1], the truncation of the perturbation series for $\frac{d\sigma_a}{d\tau}$ results in a deviation from the actual cross section that can be used to estimate the theory uncertainty. As such, we introduce seven parameters which incorporate this theory error by allowing the profile functions to vary while still satisfying their theoretical constraints. We will introduce each of them in this section.

The hard scale is constrained only by an event's center-of-mass energy, not by the particular value of thrust. We therefore use the formula

$$\mu_H(\tau) = e_H Q, \tag{2.3}$$

where e_H is chosen from the interval $[\frac{1}{2}, 2]$ and by default is set to 1. The profile parameter e_H encodes our theoretical uncertainty in the choice of hard scale.

The soft scale obeys $\mu_S \sim \Lambda_{\rm QCD}$ in the peak region. We use the formula

$$\mu_S(\tau) = \begin{cases} \mu_0, & \tau \leq t_0 \\ (\mu_0 + a(\tau - t_0)^2)(1 + e_S(\tau - t_0)^2(\tau - 1/2)^2), & t_0 \leq \tau \leq t_1 \\ (b\tau + c)(1 + e_S(\tau - t_0)^2(\tau - 1/2)^2), & t_1 \leq \tau \leq t_2 \\ (\mu_H - d(1/2 - \tau)^2)(1 + e_S(\tau - t_0)^2(\tau - 1/2)^2), & \tau \geq t_2. \end{cases} \tag{2.4}$$

where e_S is another theory parameter, which we set to 0 by default or ± 1 in our scans. The values of a, b, c, and d are fixed by imposing continuity and equality of the first derivative at all three transition points. We find

$$
\begin{aligned}
a &= \frac{\mu_H - \mu_0}{(t_1 - t_0)(t_2 - t_1 - t_0 + 1/2)}, \\
b &= \frac{2(\mu_H - \mu_0)}{t_2 - t_1 - t_0 + 1/2}, \\
c &= \frac{\mu_0(t_2 + 1) - \mu_H(t_0 + t_1)}{t_2 - t_1 - t_0 + 1/2}, \\
d &= \frac{\mu_H - \mu_0}{(1/2 - t_2)(t_2 - t_1 - t_0 + 1/2)}.
\end{aligned}
\tag{2.5}
$$

Since the width of the peak region varies with Q, we define $n_0 = t_0 Q$ and $n_1 = t_1 Q$. We determine the theoretical uncertainty associated with the τ value of these transitions by varying n_0 and n_1 rather than t_0 and t_1, because this way the variation is uniform for all center-of-mass energies. The default values of n_0 and n_1 are 2.5 GeV and 5 GeV, respectively, and both are allowed to vary up or down in our theory scans. The parameter n_0 is varied by ± 1 GeV, while n_1 is varied in the range $[3.5, 5]$ GeV. Note that we have decreased the range of variation of n_1 from that in [1], because a more careful treatment of this uncertainty is needed for the peak analysis, and in particular we must also maintain $n_0 < n_1$ without biasing our choice of parameters. Although t_2 was varied in the theory uncertainty estimates for the tail region, here we simply fix it at 0.33, as the particular value of μ_S at higher values of τ has no effect on the peak.

In [1], the flat region where $\tau < t_0$ was not included in μ_S, and instead, the parabolic region extended from $\tau = 0$ to t_1. While the parabola is fine for tail fits, this approach shifts the peak of $\frac{\mathrm{d}\sigma}{\mathrm{d}\tau}$ to the left substantially, and hence is not consistent with a proper analysis of the peak region. Physically, we interpret the necessity of the flat region as evidence that μ_S must be comparable to Λ_{QCD} not only in the limit where $\tau \to 0$, but also for sufficiently small finite values of τ, in order to correctly account for the effects of hadronization. We also find that the cross section is highly sensitive to the choice of n_0. Figure 2-1 displays it for three different choices, spaced by 1 GeV, and illustrates the necessity of the flat region.

The jet scale obeys $\mu_J \sim \sqrt{\Lambda_{\mathrm{QCD}} Q}$ in the peak region, and thus it is natural to take it to be $\sqrt{\mu_H \mu_S}$. We modify this simple formula slightly to allow variation as a

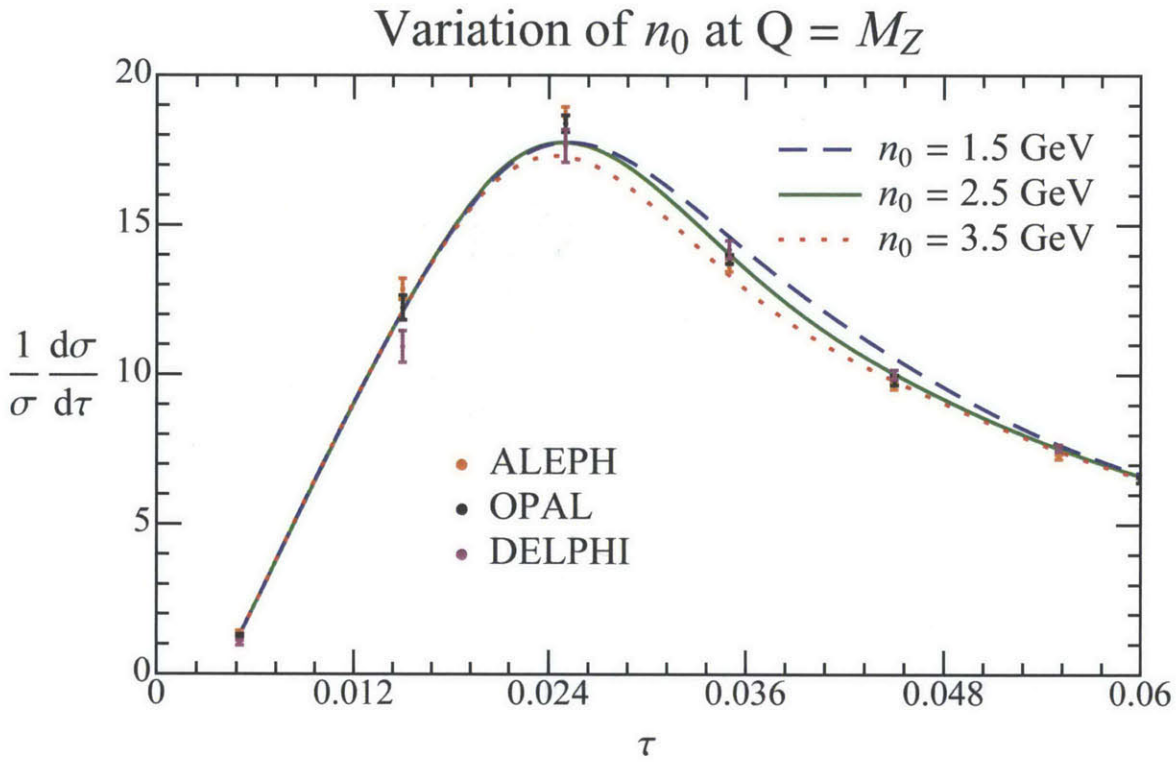

Figure 2-1: The thrust peak-region cross sections for three values of n_0, the parameter which determines the length of the flat region of $\mu_S(\tau)$, at $Q = m_Z$. Central fit values were used for the basis coefficients of the soft model function (up to c_4) to illustrate the effect of varying the parameter in isolation.

function of τ:

$$\mu_J(\tau) = \left(1 + e_J \left(\frac{1}{2} - \tau\right)^2\right) \sqrt{\mu_H \mu_S(\tau)}. \tag{2.6}$$

This equation preserves the convergence of the scales in the far-tail region while allowing significant variation of the jet scale in the peak region. We set the parameter e_J to zero by default and change it randomly to either 1 or -1 in our scan for estimating theory uncertainty. As expected, the value of μ_J in the peak region has a much smaller effect than the value of μ_S, and so the choice of e_J does not substantially change the cross section.

There is also a subtraction scale R introduced in the gap formalism, discussed below in Section 2.2. This scale must differ from μ_S at low values of τ and then join

with it to avoid summation of large logarithms at higher values of τ. Just as with μ_S, in the peak we must introduce a flat region from $\tau = 0$ to t_0. Between t_0 and t_1, in order to impose continuity and differentiability, we must insert a cubic region with no linear term; otherwise, the first derivative would be nonzero at the end of the flat region. This gives us the formula

$$R(\tau) = \begin{cases} R_0, & \tau \leq t_0 \\ R_0 + \mu_1(\tau - t_0)^2 + \mu_2(\tau - t_0)^3, & t_0 \leq \tau \leq t_1 \\ \mu_S(\tau)(1 + e_R(\tau - \tau_R)^2), & t_1 \leq \tau \leq \tau_R, \\ \mu_S(\tau), & \tau \geq \tau_R. \end{cases} \tag{2.7}$$

Here e_R is another varied in our scans (0 by default and varied to ± 1), but τ_R is fixed to 0.25. Imposing continuity and differentiability at t_1 gives us the values of μ_1 and μ_2 (when e_R is set to 0):

$$\begin{aligned} \mu_1 &= \frac{3\mu_0 + a\ t_0^2 - 2\ a\ t_0\ t_1 + a\ t_1^2}{(t_1 - t_0)^2}, \\ \mu_2 &= -\frac{2\mu_0}{(t_1 - t_0)^3}, \end{aligned} \tag{2.8}$$

with a given by Eq. (2.5). The profile functions μ_H, μ_J, μ_S, and R, with their default parameter values, are displayed in Figure 2-2.

There is also a scale $\mu_{\rm ns}$ governing the resummation of logarithms of τ in the nonsingular terms. To account for uncertainty in this resummation, we allow it to have three possible values, given by

$$\mu_{\rm ns}(\tau) = \begin{cases} \mu_H, & n_s = 1 \\ \mu_J(\tau), & n_s = 0 \\ \frac{1}{2}(\mu_J(\tau) + \mu_S(\tau)), & n_s = -1. \end{cases} \tag{2.9}$$

For peak fits we take $n_s = 1$ by default rather than $n_s = 0$, because we find that this value is much more consistent with the experimental data. We still allow n_s to take on other values in our theory scan, but employ a weighting system to devalue choices

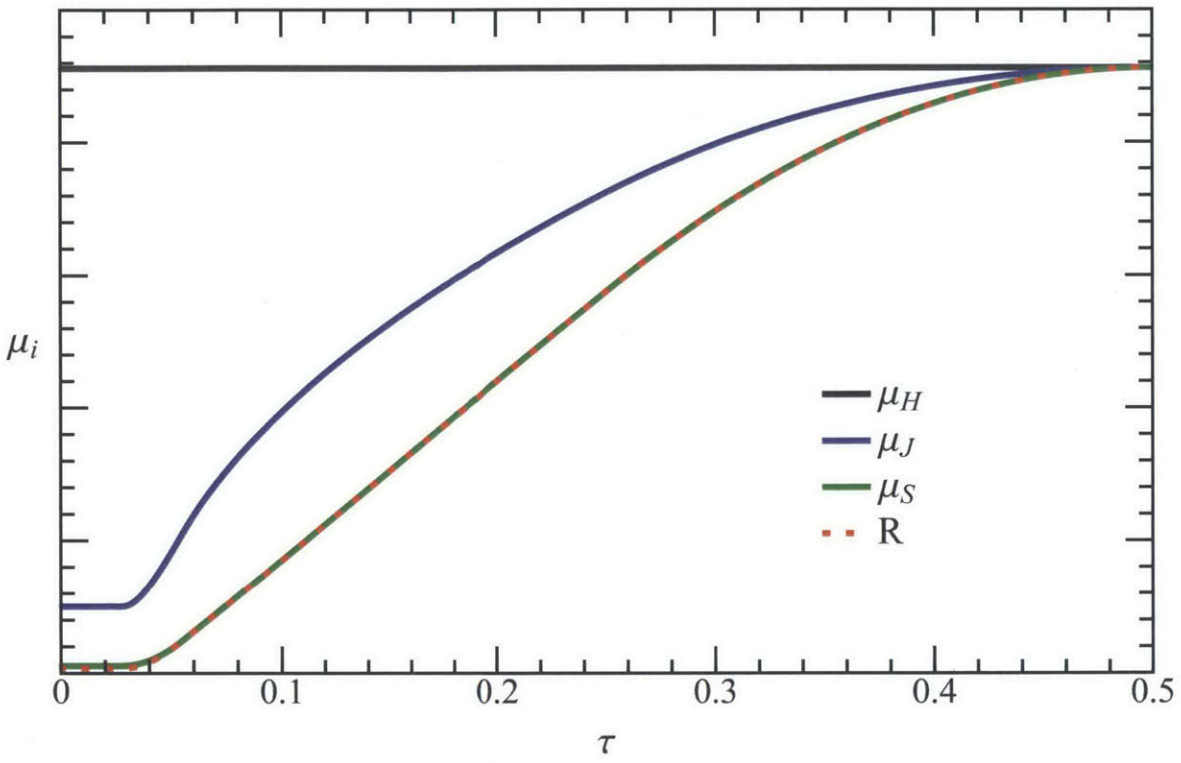

Figure 2-2: The profile functions, with theory parameters set to their default values.

of theory parameters that are obviously inconsistent with experiment. More detail is provided in Chapter 4.

2.3 The Gap Formalism

An important feature of the factorization formula presented in [1] is a subtraction scheme that removes an $\mathcal{O}(\Lambda_{\rm QCD})$ renormalon from the matrix element $\bar{\Omega}_1$ present in the $\overline{\rm MS}$ scheme. We refer to this subtraction scheme as the R-gap scheme, and it has a significant effect on our determination of the soft function's moments. Without subtracting the renormalon the soft model function would depend largely on the order in perturbation theory to which the cross section is calculated. Hence, here we shall summarize it briefly. The approach presented here is based on results originally derived in [2].

In the $\overline{\text{MS}}$ scheme, the soft function is defined as a convolution of partonic and nonperturbative components, written as

$$S_\tau(k,\mu) = \int \mathrm{d}k' S^\tau_{\text{part}}(k-k',\mu) S^\tau_{\text{mod}}(k'). \tag{2.10}$$

Here the moments of S^{mod}_τ are defined by

$$2^i \bar{\Omega}_i = \int \mathrm{d}k\ k^i\ S^\tau_{\text{mod}}(k). \tag{2.11}$$

We introduce a gap parameter Δ, such that $S^\tau_{\text{mod}}(k) \to S^\tau_{\text{mod}}(k-2\Delta)$. The parameter Δ contains the complete renormalon ambiguity, and we may split it into a perturbative and nonperturbative component, writing

$$\Delta = \bar{\Delta}(R,\mu_S) + \delta(R,\mu_S), \tag{2.12}$$

where $\bar{\Delta}(R,\mu_S)$ is a nonperturbative renormalon-free parameter, and $\delta(R,\mu_S)$ is a perturbative series. The parameter Δ is subtraction-scheme independent, while its components depend on the choice of subtraction scheme, hence the necessity of the profile function $R(\tau)$ defined in section 2.2. We can then write the soft function as

$$S(\ell,\mu_S) = \int \mathrm{d}\ell' \left[e^{-2\delta(R,\mu_S)\partial/\partial\ell} S_{\text{part}}(\ell-\ell',\mu_S)\right] S^{\text{mod}}_\tau(\ell' - 2\bar{\Delta}(R,\mu_S)). \tag{2.13}$$

The derivative acting on S_{part} gives a renormalon free perturbative soft result from the term in square brackets. The moments of the soft function are also now renormalon free and given by

$$2^i \Omega_i(R,\mu_S) = \int \mathrm{d}k\ k^i\ S^\tau_{\text{mod}}(k - 2\bar{\Delta}). \tag{2.14}$$

The Ω_i quoted in our fits are thus subtraction-scheme dependent but free of the renormalon which would render them numerically unstable and highly dependent on the order in perturbation theory.

Chapter 3

Nonperturbative Components

The soft model function incorporates nonperturbative effects into the factorization formula for thrust. It accounts for the uniform soft-gluon radiation which leads to soft hadrons in between and within jets, which is not included in perturbation theory. It must be normalized, positive definite, and have support for $k \geq 0$. Rather than choosing a particular analytic ansatz for S^{τ}_{mod}, we represent it as a linear combination of basis functions, which are chosen to satisfy all its known properties. This approach allows us the flexibility to learn more about the function by incorporating successively more basis functions. Following the approach of [9], we write

$$S_{\tau}^{\mathrm{mod}}(k, \lambda, \{c_i\}) = \frac{1}{\lambda}\left[\sum_{n=0}^{\infty} c_n f_n\left(\frac{k}{\lambda}\right)\right]^2, \tag{3.1}$$

where

$$f_n(z) = 8\sqrt{\frac{2z^3(2n+1)}{3}}e^{-2z}P_n\left(g(z)\right) \tag{3.2}$$

and

$$g(z) = \frac{2}{3}\left(3 - e^{-4z}(3 + 12z + 24z^2 + 32z^3)\right) - 1. \tag{3.3}$$

Here P_n are the Legendre polynomials. The basis functions $f_n(k/\lambda)$ are displayed in Figure 3-1 for reference. We always choose $\{c_i\}$ such that $\sum_i c_i^2 = 1$, which ensures

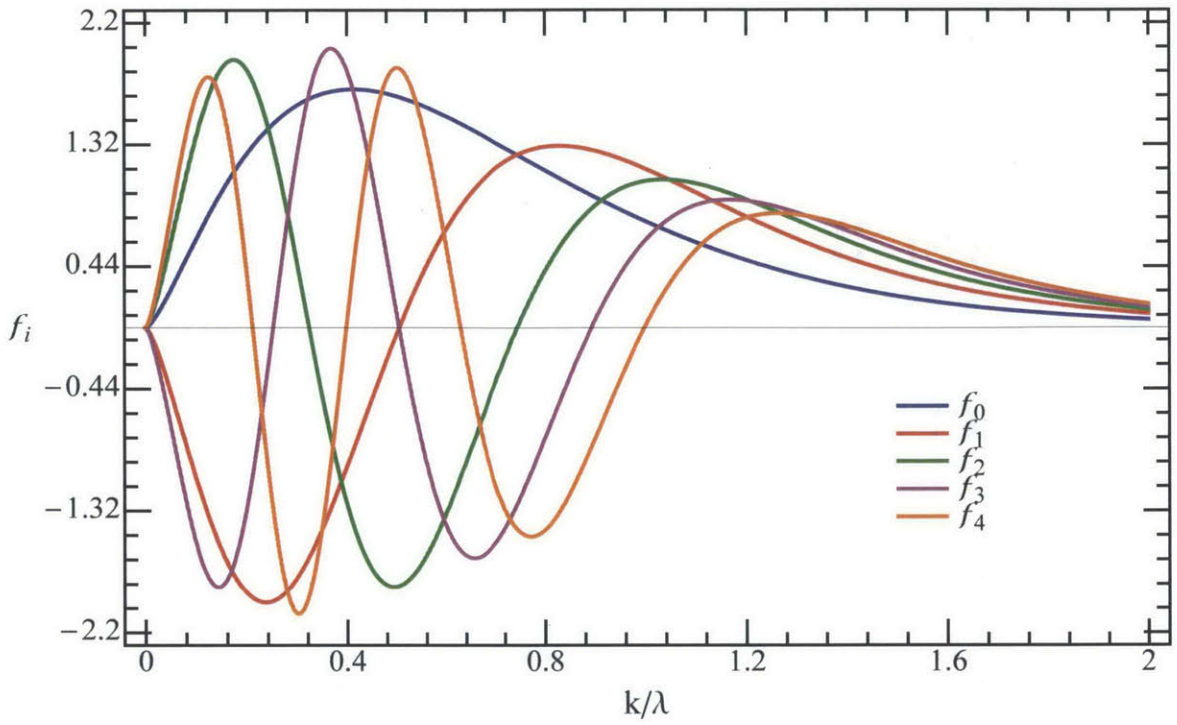

Figure 3-1: The basis functions f_i.

the proper normalization, $\int \mathrm{d}k\ S^{\tau}_{\mathrm{mod}}(k) = 1$. Our code supports calculations of $\frac{\mathrm{d}\sigma}{\mathrm{d}\tau}$ with basis coefficients from c_0 up to c_4, allowing us the freedom to determine the first through fourth moments of the soft model function. In our fits we treat S^{τ}_{mod} as a function of c_1 through c_4 and determine c_0 to satisfy the normalization constraint. Thus, we are able to explore the soft model function in a four dimensional parameter space, which may be viewed from either the perspective of basis coefficients c_i or moments Ω_i.

The parameter λ would be redundant if the infinite sum over all basis functions could be carried out, but due to the truncation of the series, it instead acts as a significant basis-selection parameter. Higher values of λ shift the peaks of the basis functions to larger values of k, while decreasing their heights to maintain normalization. Using the first five basis functions, only certain values of λ provide fast enough convergence to achieve good fits to the data. We use the default value $\lambda = 0.55$ GeV, although we show that a wider range of values are all acceptable in Section 4.1. Inside

this range, the best-fit values of the coefficients c_i change as λ is varied, but the values of the moments Ω_i remain consistent. This result is sensible, as we should require different proportions of the functions in a different basis to achieve a function with the same physical consequences, which are encoded in the moments. Outside the preferred range of λ, the minimum χ^2 value increases, and both the basis coefficients and the moments vary with λ, indicating poor convergence. In the tail fits from [1], λ was varied in place of c_1 in order to effectively vary the first moment Ω_1. We are reassured by the fact that the best-fit value of λ from those fits falls within the range of acceptable values for our peak analysis. We also find that tail fits in which lambda is fixed at 0.55 GeV and c_1 is varied reproduce the results of [1] for the central profiles.

We determine formulae for the Ω_i in terms of the basis coefficients c_i by using Equation 2.14, resulting in the following formulae:

$$\begin{aligned}
\Omega_1 &= \bar{\Delta} + \frac{\lambda}{2}\,\tilde{\Omega}_1, \\
\Omega_2 &= \bar{\Delta}^2 + \lambda\,\bar{\Delta}\,\tilde{\Omega}_1 + \frac{\lambda^2}{4}\,\tilde{\Omega}_2, \\
\Omega_3 &= \bar{\Delta}^3 + 3\bar{\Delta}^2\,\frac{\lambda}{2}\,\tilde{\Omega}_1 + 3\,\bar{\Delta}\,\frac{\lambda^2}{4}\,\tilde{\Omega}_2 + \frac{\lambda^3}{8}\,\tilde{\Omega}_3, \\
\Omega_4 &= \bar{\Delta}^4 + 2\,\bar{\Delta}^3\,\lambda\,\tilde{\Omega}_1 + 3\,\bar{\Delta}^2\,\frac{\lambda^2}{2}\,\tilde{\Omega}_2 + \bar{\Delta}\,\frac{\lambda^3}{2}\,\tilde{\Omega}_1 + \frac{\lambda^4}{16}\,\tilde{\Omega}_4,
\end{aligned} \tag{3.4}$$

where we determine the $\tilde{\Omega}_i$ by integrating over the soft functions produced by setting c_i terms to nonzero values. Recall that the gap formalism introduces the parameter $\bar{\Delta} = \bar{\Delta}(\mu_0, R_0)$, such that the soft function entering the factorization formula is actually shifted in k-space. This shift results in the moments having $\bar{\Delta}$ dependence, effectively adding another fit parameter to the soft function. However, in practice we find that the choice $\bar{\Delta}$ has little effect on the fit values of the moments, as the c_i shift to compensate for changes in $\bar{\Delta}$. As such, we fix $\bar{\Delta} = 0.025$ GeV. The terms $\tilde{\Omega}_i$, which give the moments of the unshifted soft function, are

$$
\begin{aligned}
\tilde{\Omega}_1 &= c_0^2 + 1.090c_1^2 + 1.100c_2^2 + 1.103c_3^2 + 1.105c_4^2 + 0.947c_0c_1 + 0.201c_0c_2 \\
&\quad + 0.190c_0c_3 + 0.084c_0c_4 + 1.014c_1c_2 + 0.250c_1c_3 + 0.242c_1c_4 + 1.019c_2c_3 \\
&\quad + 0.263c_2c_4 + 1.020c_3c_4, \\
\tilde{\Omega}_2 &= 1.25c_0^2 + 1.713c_1^2 + 1.789c_2^2 + 1.817c_3^2 + 1.831c_4^2 + 2.131c_0c_1 + 1.036c_0c_2 \\
&\quad + 0.694c_0c_3 + 0.484c_0c_4 + 2.516c_1c_2 + 1.333c_1c_3 + 0.937c_1c_4 + 2.609c_2c_3 \\
&\quad + 1.422c_2c_4 + 2.649c_3c_4, \\
\tilde{\Omega}_3 &= 1.875c_0^2 + 3.226c_1^2 + 3.579c_2^2 + 3.741c_3^2 + 3.834c_4^2 + 4.262c_0c_1 + 3.020c_0c_2 \\
&\quad + 2.211c_0c_3 + 1.726c_0c_4 + 5.755c_1c_2 + 4.159c_1c_3 + 3.152c_1c_4 + 6.255c_2c_3 \\
&\quad + 4.587c_2c_4 + 6.510c_3c_4, \\
\tilde{\Omega}_4 &= 3.281c_0^2 + 6.747c_1^2 + 8.086c_2^2 + 8.800c_3^2 + 9.251c_4^2 + 8.791c_0c_1 + 7.749c_0c_2 \\
&\quad + 6.431c_0c_3 + 5.435c_0c_4 + 13.512c_1c_2 + 11.550c_1c_3 + 9.690c_1c_4 + 15.534c_2c_3 \\
&\quad + 13.272c_2c_4 + 16.698c_3c_4.
\end{aligned}
\tag{3.5}
$$

Unfortunately, it is not possible to invert these equations to obtain $c_i(\Omega_i)$ in order to write the soft function as a function of its moments, since polynomial equations have multiple solutions. Instead, we must perform fits in c-space and determine the values of the moments by these equations, propagating uncertainties through them. See Section 4.5 for more information.

The values of the higher moments are highly constrained by the values of the lower moments, independently of fits to the data. For instance, the second moment must satisfy the Cauchy-Schwarz inequality $\Omega_2/\Omega_1^2 \geq 1$. As such, when examining the correlations between moments, as we do in our theory uncertainty scans, it is more illustrative to work with the cumulant moments Ω_i',

$$
\begin{aligned}
\Omega_1' &= \Omega_1, \\
\Omega_2' &= \Omega_2 - \Omega_1^2, \\
\Omega_3' &= \Omega_3 - 3\Omega_2\ \Omega_1 + 2\Omega_1^3, \\
\Omega_4' &= \Omega_4 - 4\Omega_3\ \Omega_1 - 3\Omega_2^2 + 12\Omega_2\ \Omega_1^2 - 6\Omega_1^4.
\end{aligned}
\tag{3.6}
$$

The higher cumulant moments are not affected by constraints in the same way the Ω_i are. They are also intuitively simpler quantities familiar from statistics; Ω_1' is the mean of the distribution, Ω_2' is the standard deviation, and Ω_3' the is skewness. Figure 3-2 illustrates the behavior of the cumulant moments when the basis coefficients vary about their central fit values. The fact that each moment behaves in a different way illustrates the fact that our fit for the c_i is related to a fit for the moment Ω_i'. We quote best-fit values and experimental uncertainties on the c_i, the Ω_i, and the Ω_i' for $i = 1, 2, 3, 4$, along with theory uncertainties on the Ω_i'.

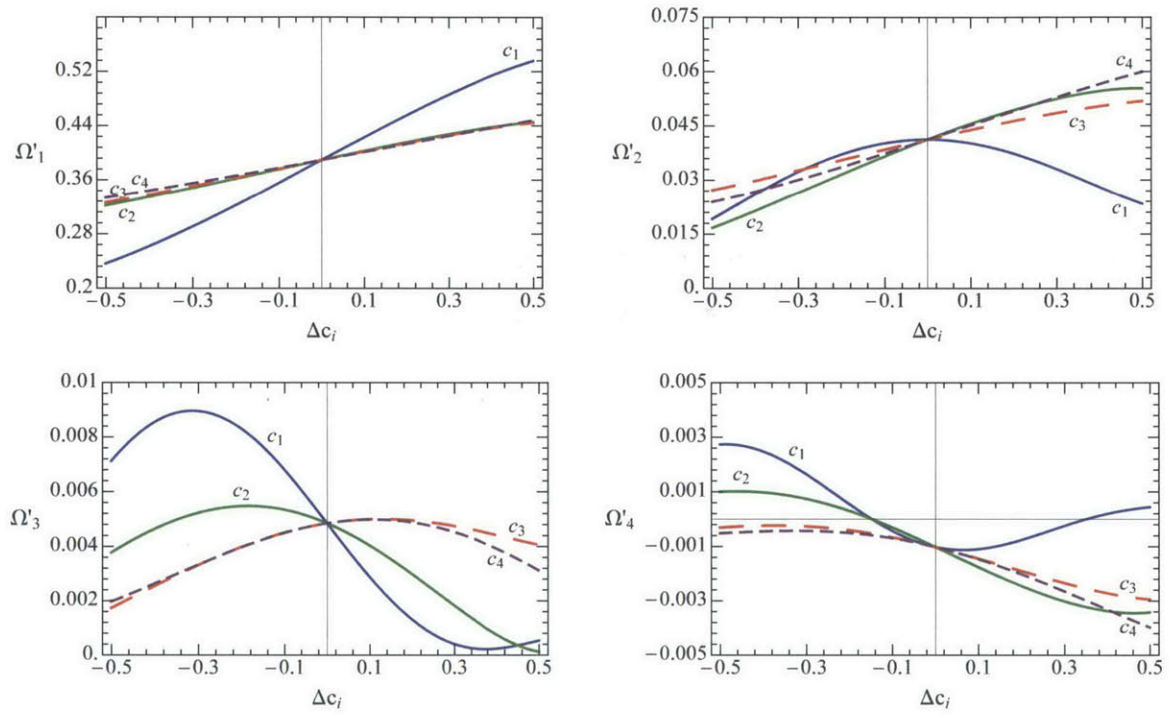

Figure 3-2: How the Ω_i' change with variations of c_i. By default c_0 is set to $\sqrt{1-\Sigma c_i^2}$ when c_i is being varied, and all other c_j are set to their central fit values using default theory parameters. The x-axis measures how far the c_i being varied deviates from its fit value.

Chapter 4

Numerical Analysis

We use thrust data from the LEP experiments ALEPH, OPAL, L3, and DELPHI, along with SLD from SLAC, JADE and TASSO from DESY, and AMY from KEK in our analyses, with Q values varying from 35 to 207 GeV. Data from $Q = 14$ and 22 GeV is also available from TASSO, but we exclude it, because at these energies the bottom quark mass is large enough that it must be treated in a more sophisticated way. Since the default data set in [1] took $\tau = 6/Q$ as the boundary between the peak and tail regions, for peak region fits, we use data in the range $[0, 6/Q]$ by default in order to analyze an independent dataset. The data is binned, and we keep all bins whose midpoint falls below the maximum allowed value of τ. We include the following center of mass energies from each data set: $Q = \{91.2, 133, 161, 172, 183, 189, 200, 206\}$ GeV from ALEPH [23], $Q = \{91, 133, 161, 172, 177, 183, 189, 197\}$ GeV from OPAL [20, 21, 22], $Q =$\{41.4, 55.3, 65.4, 75.7, 82.3, 85.1, 91.2, 130.1, 136.1, 161.3, 172.3, 182.8, 188.6, 194.4, 200.0, 206.2\} GeV from L3 [14, 15], $Q =$\{45, 66, 76, 89.5, 91.2, 93, 133, 161, 172, 183, 189, 192, 196, 200, 202, 205, 207\} GeV from DELPHI [16, 17, 18, 19], $Q = 91.2$ GeV from SLC [13], $Q = \{35, 44\}$ from JADE [12], $Q = \{35, 44\}$ GeV from TASSO [10], and $Q = 55.2$ GeV from [11].

In order to compare the binned data with our theoretical distribution for $\frac{1}{\sigma}\frac{d\sigma}{d\tau}$, it is necessary to integrate the distribution over the τ values spanned by each bin. To perform the peak fits we use a χ^2 minimization procedure in four-dimensional c_i-space (with the additional basis coefficient, c_0, fixed by normalization), with α_s

fixed by its tail-fit value. We justify the decision to fix α_s by noting that when fits are performed at a wide range of fixed α_s values, the moments Ω_i and the minimum χ^2 value vary slowly, on an order significantly greater than the 1σ uncertainty in α_s from the tail region fits. The tail region fixes α_s more precisely, while the peak region fixes the moments of the soft model function. We discuss this decision in more detail in Section 4.3.

In practice, we compute the values of the coefficients of each c_i^2 and $c_i c_j$ term appearing in the integral of $\frac{1}{\sigma}\frac{\mathrm{d}\sigma}{\mathrm{d}\tau}$ over the τ range for each bin in our collective dataset. We then compute $\chi^2(c_1, c_2, c_3, c_4)$ using an inverse correlation matrix. The diagonal terms of the correlation matrix contain the statistical and systematic uncertainties for each bin, added in quadrature. Given the lack of information about correlations between bins in the experimental results, we use two different models for the off-diagonal terms of the matrix. The simpler of the two, which we refer to as the *uncorrelated* method, assumes that the systematic uncertainties associated with each bin are independent of each other. The *minimal overlap* method assumes that the systematic uncertainties associated with each bin are positively correlated, but it conservatively estimates the amount by which they are correlated using the formula $\sigma_{ij} = \min[\Delta_i^{\mathrm{sys}}, \Delta_j^{\mathrm{sys}}]^2$. By default, tail fits from [1] used the minimal overlap method. However, in the peak region we find that this method leads to erratic behavior in the best fit with variations of α_s and may not be appropriate. As such, we use the uncorrelated method for our peak fits, although the minimal overlap method is used to ensure consistency with the tail, as described in Section 4.4.

For many choices of theory parameters, the χ^2 function in four-dimensional c-space contains local minima. Unfortunately, imposing normalization with c_0 introduces square roots and makes it intractable to solve the system of equations resulting from setting the partial derivative of χ^2 with respect to each c_i to zero. Instead, we employ a minimization algorithm, which takes care to avoid becoming trapped in a local minimum. We initially use a grid-search approach which samples the c-space on a uniform four-dimensional grid and then runs a simple gradient-based minimization algorithm from the minimum point sampled. Theoretically, this approach is guar-

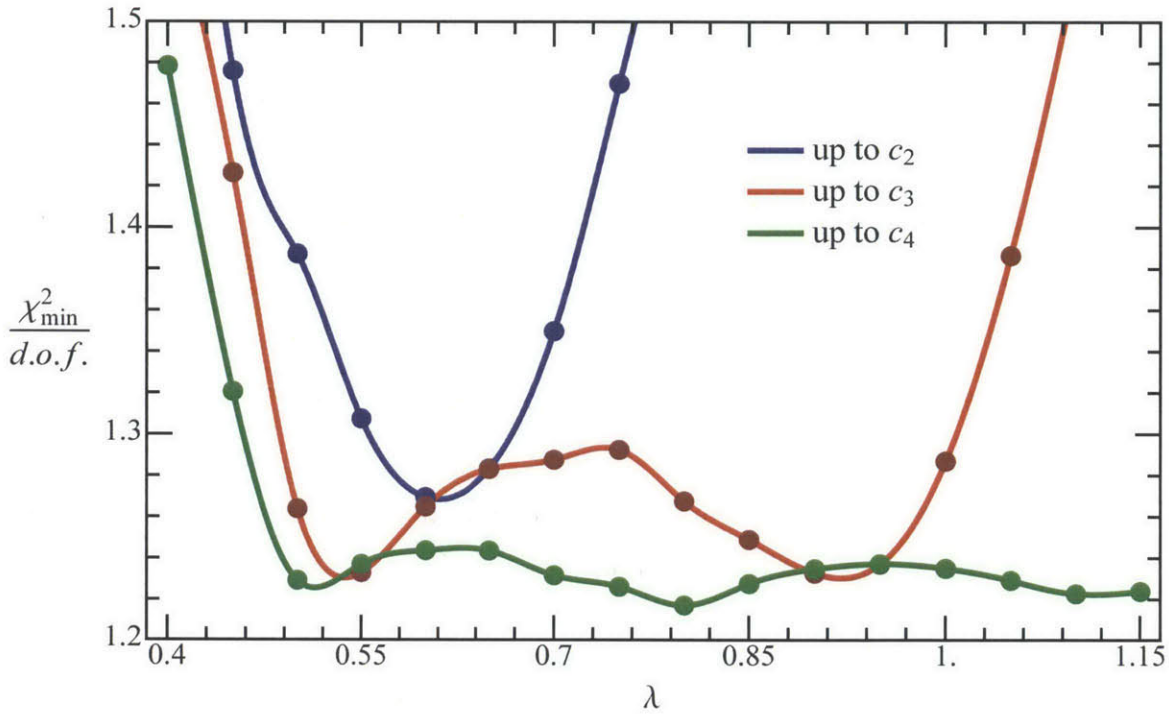

Figure 4-1: Minimum χ^2 values for different choices of λ. Including more basis functions increases the range of λ over which a good fit to the experimental data is possible.

anteed to succeed for a sufficiently fine grid. We restrict our grid to the 4-sphere centered at $c_1 = c_2 = c_3 = c_4 = 0$ with $r = 0.64$ in order to ensure that f_0 is the dominant basis function. This choice helps ensure that the fitting algorithm selects a minimum in c-space for which the fit converges quickly enough to a reasonable soft function.

4.1 Choice of Basis

As described in Chapter 3, the soft function is represented by a linear combination of normalized basis functions whose width is characterized by a parameter λ. In principle this parameter is redundant, because the soft function can be written as an infinite sum of basis functions for any choice of λ. However, in order to characterize the soft function by fitting to the data, we must truncate this sum. For computational reasons we use only the first five basis functions, fitting the coefficients c_1 through c_4

and adjusting the value of c_0 to impose normalization. As such, only certain choices of λ provide fast enough convergence to the best fit soft function.

We find that a wide range of λ values, the lowest being 0.5 GeV, give comparable fits when basis functions up to f_4 are included. A plot of the best-fit value of χ^2 at varied λ for fits up to c_2, c_3, c_4 is displayed in Figure 4-1. This plot makes evident the weakening of the dependence on λ as higher c_i are included in the fit. Once c_4 is included, any choice of λ between 0.5 and 1.15 GeV gives a comparably good fit. (At higher values of λ the minimization algorithm fails to converge, and so an upper bound on good choices of λ cannot be given at this time.)

For our peak fits with any choice of profiles parameters, we choose $\lambda = 0.55$ GeV. Although this value does not give the absolute minimum χ^2, it is a convenient choice, as at this value χ^2_{min}/d.o.f. does not decrease significantly when c_4 is included in the fit. As such, the uncertainty in c_4 in this basis can be thought of as accounting for the truncation uncertainty in the series. Although both $\lambda = 0.55$ and 0.9 GeV satisfy this criterion, $\lambda = 0.55$ GeV is approximately the value obtained in previous tail-fits in which λ, as opposed to c_1, was treated as the fit parameter, so we use the same value for convenience.

In addition to λ, the soft function is determined by the parameter $\bar{\Delta}$, which shifts the function to the right as part of the gap formalism (see Section 2.3). Although $\bar{\Delta}$ could be treated as a fit parameter, in practice we find that the choice of $\bar{\Delta}$ has little effect on the best-fit values of the moments. By default we take $\bar{\Delta}$ to be 0.025 GeV, which is slightly lower than the 0.05 GeV previously used for tail fits. When we vary $\bar{\Delta}$ by 0.025 GeV we find that the differential cross section changes imperceptibly, but 0.025 GeV gives a slightly better minimum χ^2 (1.22 when 0.025 GeV is used and 1.23 when 0.05 GeV is used). The best-fit values of the basis coefficients, however, vary significantly, as does the shape of the soft function. More details on the consistency of these two observations will be given in Section 4.6.

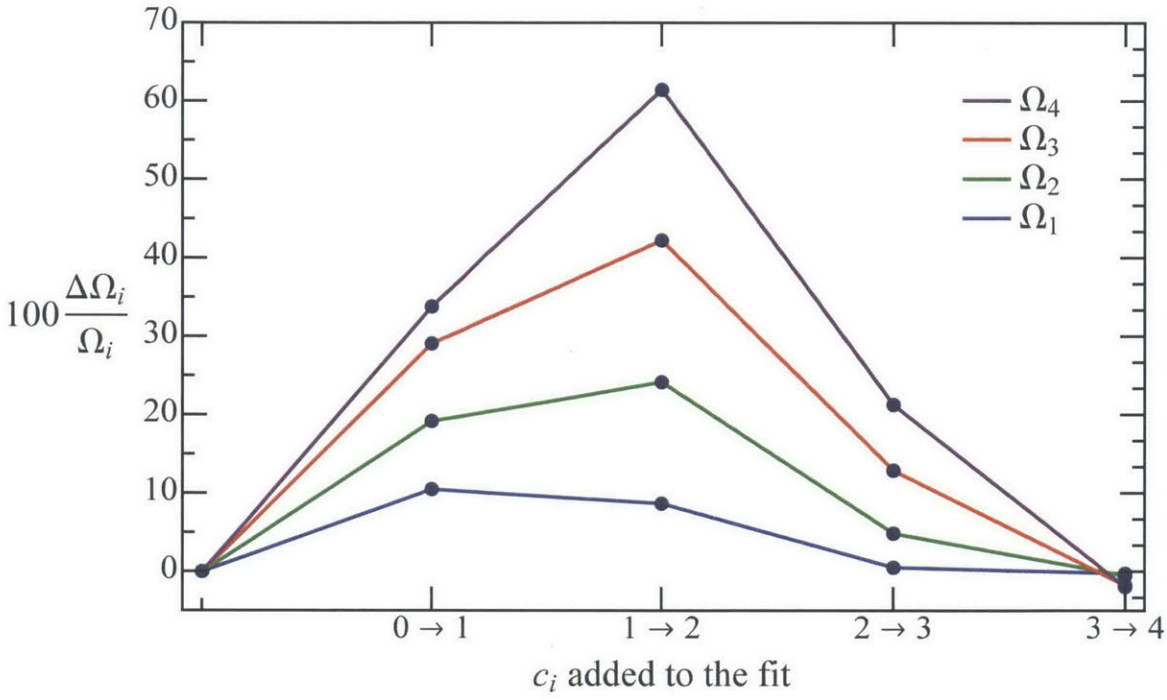

Figure 4-2: The percent each Ω_i increases or decreases when higher basis functions are added.

4.2 Number of Basis Functions

We performed fits with two, three, four, and five basis functions included. To use fewer than five basis functions, we simply set $c_i = 0$ for $i > n$, where n corresponds to the highest order function included. The overall χ^2 value decreases with each new function included; for central profile fits up to c_1, c_2, c_3, and c_4, respectively, we find minimum χ^2 values of 480.0, 259.5, 247.2, and 241.7. Dividing by the number of degrees of freedom, with 202 bins included in the fit by default, these correspond to minimum values of

$$\frac{\chi^2_{\text{min}}}{\text{d.o.f.}} = \begin{cases} 2.42, \text{up to } c_1, \\ 1.31, \text{up to } c_2, \\ 1.25, \text{up to } c_3, \\ 1.23, \text{up to } c_4. \end{cases} \tag{4.1}$$

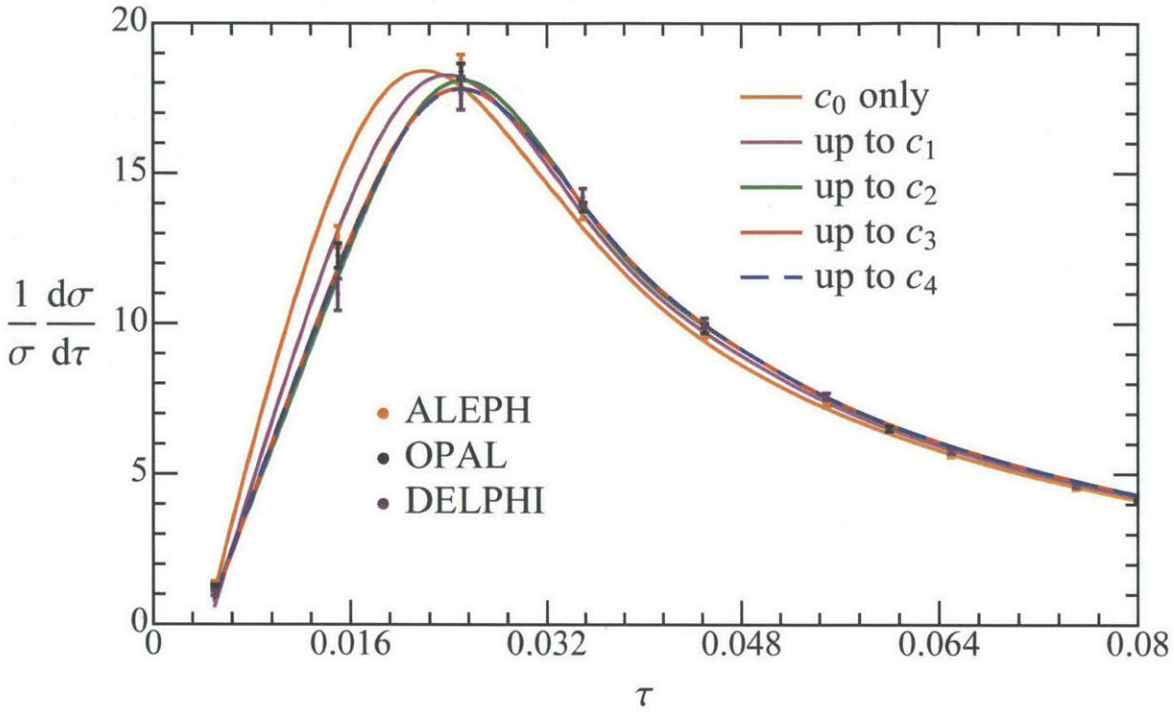

Figure 4-3: The best-fit cross section as higher basis functions are added.

The decrease in difference between minimum χ^2 values as higher c_i are included indicates that the fit is more sensitive to the lower moments than the higher ones, as expected. Figure 4-2 displays the relative changes in the size of each moment as basis functions are added to the fit. It is clear that including c_2 has the greatest impact not only on the best-fit χ^2 value, but also on each of the moments Ω_i.

The resulting cross sections (including one for which c_0 is simply set to 1) at $Q = m_Z$ are displayed in Figure 4-3. This plot makes it apparent that most of the decrease in χ^2 comes from the ability of the fit to reach the data in the first few bins. Physically, this corresponds to the measurable effects of hadronization increasing for thinner jets. The rightward shift as higher moments are properly accounted for is also expected, because the broadening due to uniform soft radiation should cause fewer events to occur as τ approaches zero. It should be noted that the cross section in the first bin, from $\tau = 0$ to 0.01, is sensitive to the inclusion of bottom quark mass effects, which are not included here.

The soft functions corresponding to the cross sections in Figure 4-3 are displayed

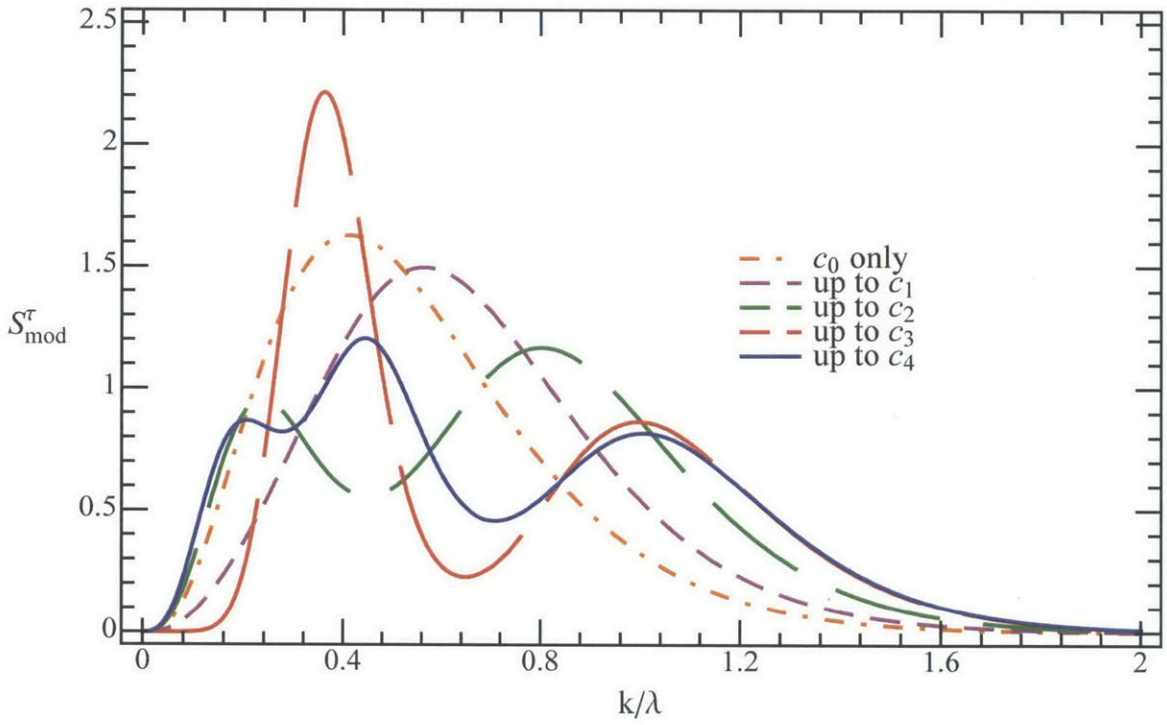

Figure 4-4: The best-fit soft function as higher basis functions are added.

in Figure 4-4. Convergence is less obvious from this plot than from the cross sections and χ^2 values, and it is possible that the shape of the soft function could change significantly upon inclusion of a higher basis function such as f_5 in the fit. We emphasize that the structure of the best-fit soft function over small changes in momenta does *not* characterize the true shape of the soft function. Instead, the *moments* of the best-fit soft function approximate the moments of the true soft function, giving a bulk representation of the shape. An infinite number of functions with identical moments up to Ω_4 could give equivalent fits, as the data is not sensitive enough to determine the higher moments and differentiate between these functions. To illustrate this point, we construct a reasonably-shaped momentum-space distribution without oscillatory behavior, project it onto the basis functions f_0 through f_4, and display the fit using the resulting soft function against our best fit in Section 4.6.

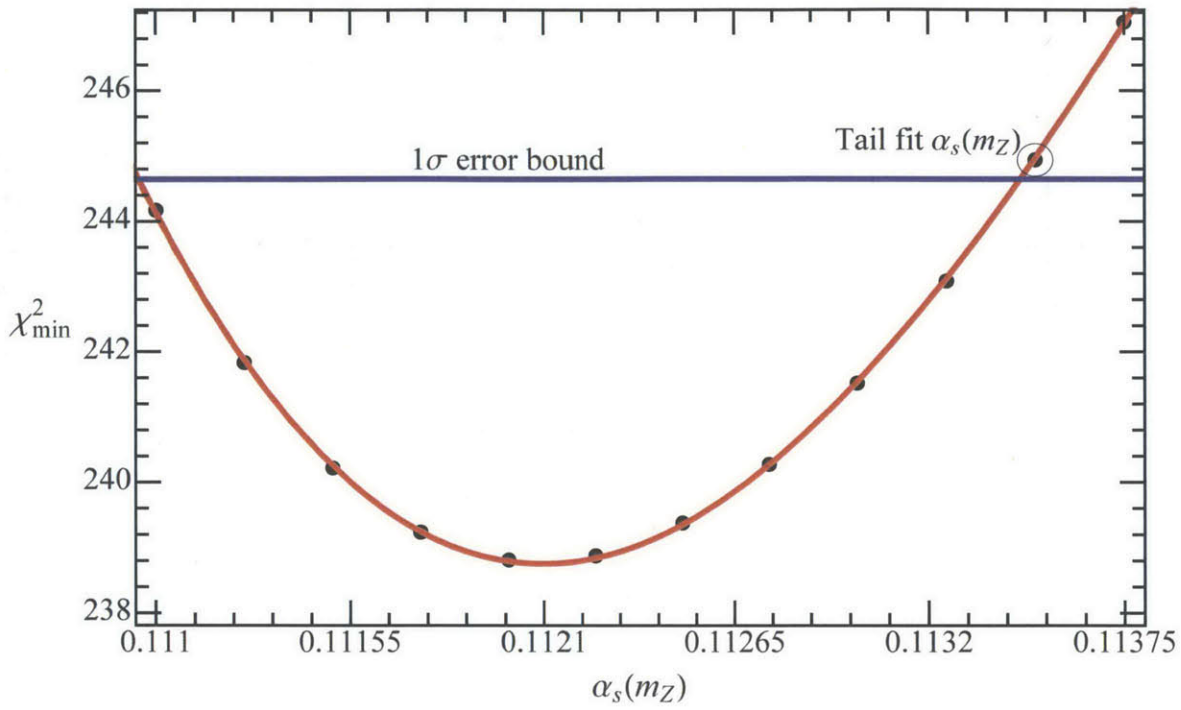

Figure 4-5: Varied α_s minimum χ^2 values. A polynomial best-fit to the points is included with a cubic term to account for the slight asymmetry about the minimum.

4.3 Variation of α_s

In our peak fits we fix the value of α_s to its best-fit value from the tail. The value of $\alpha_s(m_Z)$ is determined much more precisely by the tail fits, since the cross section there is sensitive to only a single moment of the soft function, Ω_1. For the central profiles, [1] found $\alpha_s(m_Z) = 0.1135 \pm (0.0002)_{\text{experiment}} \pm (0.0005)_{\text{hadronization}} \pm (0.0009)_{\text{perturbative}}$. Taking the uncertainties to be uncorrelated, this gives a total 1σ error of approximately 0.0010. For comparison, a plot of the minimal χ^2 value for fits in c_i-space for various values of $\alpha_s(m_Z)$ is displayed in Figure 4-5. The 1σ uncertainty in α_s in the peak due to experiment and hadronization, but not yet accounting for perturbative parameter variations, is approximately 0.0012. Here the value with only experimental uncertainty is already larger than the tail's 1σ limit including theory uncertainties. We exploit this fact by fixing $\alpha_s(m_Z)$ in the peak region to the value determined in the tail, which greatly improves the efficiency of our fits.

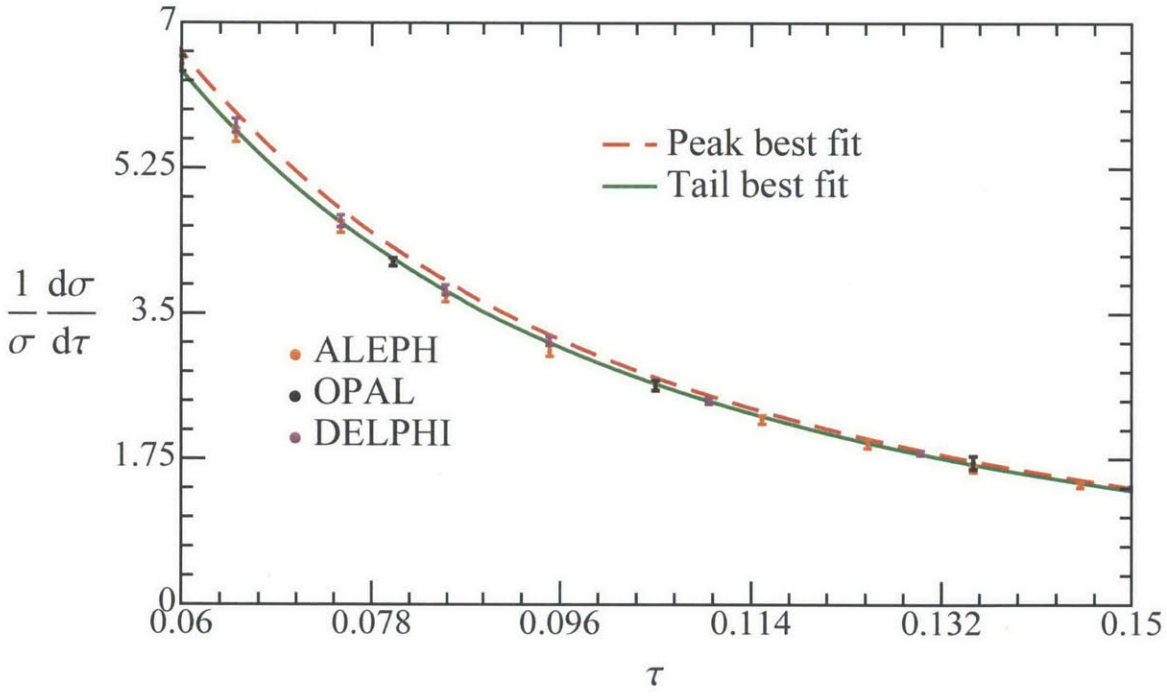

Figure 4-6: A comparison of the best fits produced from peak and tail data in the tail region.

4.4 Choice of Data

By default, we define the end of the peak region to be $6/Q$ for purposes of inclusion of data in the fit. When this value is contained between a bin's endpoints, we keep the bin if its median τ value is less than or equal to $6/Q$ and throw it out if it is greater. The choice of $6/Q$ matches the definition of the tail region in [1], and so we make the same default choice for consistency. Note, however, that the best fit cross section does systematically deviate above the first few bins of the tail region when this choice is made. Figure 4-6 illustrates this deviation.

Although this deviation may appear problematic, taking into account the correlations between uncertainties in the bins, it does not have a serious impact on our results. In Figure 4-7 we compare the results of the minimal overlap method and the uncorrelated method as we include higher τ data in the fit. Without allowing for correlations between the systematic uncertainties, we see that Ω_1 is driven down by the tail data and the minimum χ^2/d.o.f. initially increases, which would naively indi-

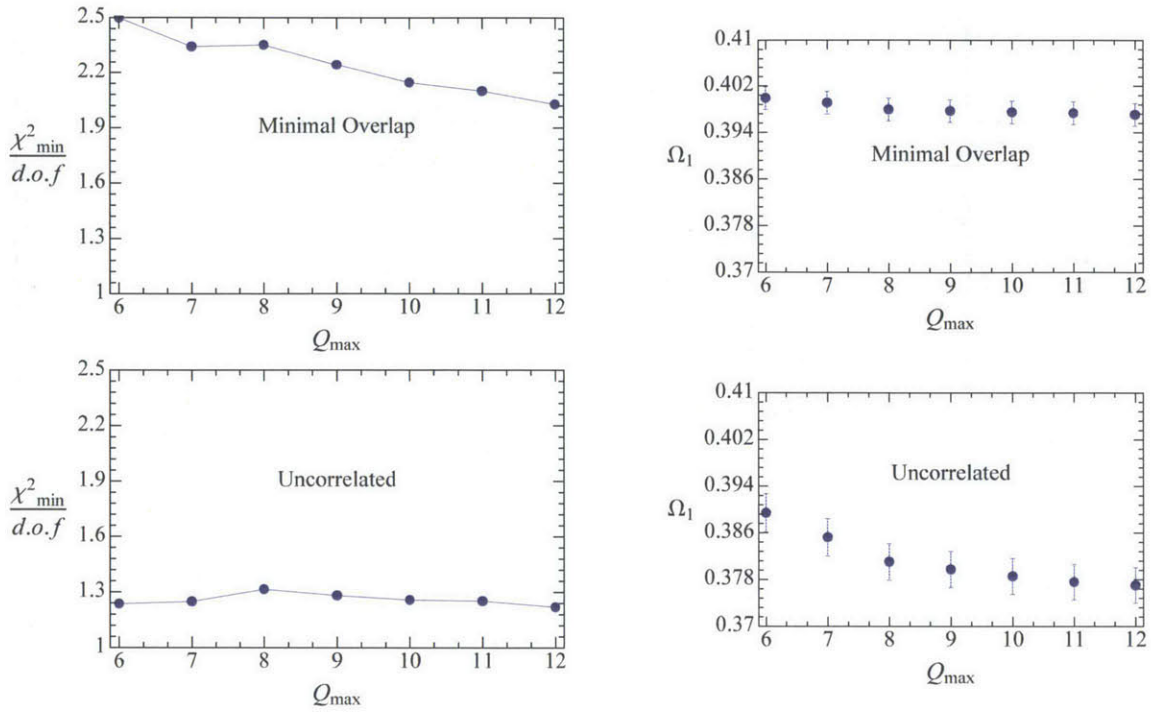

Figure 4-7: A comparison, between the uncorrelated and minimal overlap methods, of how the minimum χ^2 value and Ω_1, measured in GeV, change as a function of how much data is included in the fit. The parameter $Q_{\max}$, also measured in GeV, determines the cutoff point, where $\tau_{\text{cutoff}} = Q_{\max}/Q$. Uncertainties in Ω_1 denote just the experimental uncertainty, without taking into account uncertainty due to higher moments. The higher Ω_i behave similarly to Ω_1 for both methods and therefore are not displayed.

cate a lack of consistency between the peak and tail's requirements for Ω_1. Allowing for correlations, however, we see that the minimum value of χ^2/d.o.f. consistently decreases, and Ω_1 is driven downwards only slightly, within the experimental uncertainty from the fit. We therefore conclude that we can continue to use $6/Q$ as the upper end of the peak region for inclusion of data in the fit.

We also note that the minimal overlap method consistently gives a higher best fit Ω_1 by as much as 0.15 GeV. The uncorrelated method gives an Ω_1 that is only slightly greater than 1σ above the tail-fit value of 0.323 ± 0.052 GeV in [1] and hence is more consistent with the tail analysis. We take this observation as farther evidence that the minimal overlap method does not properly handle correlations in the peak region.

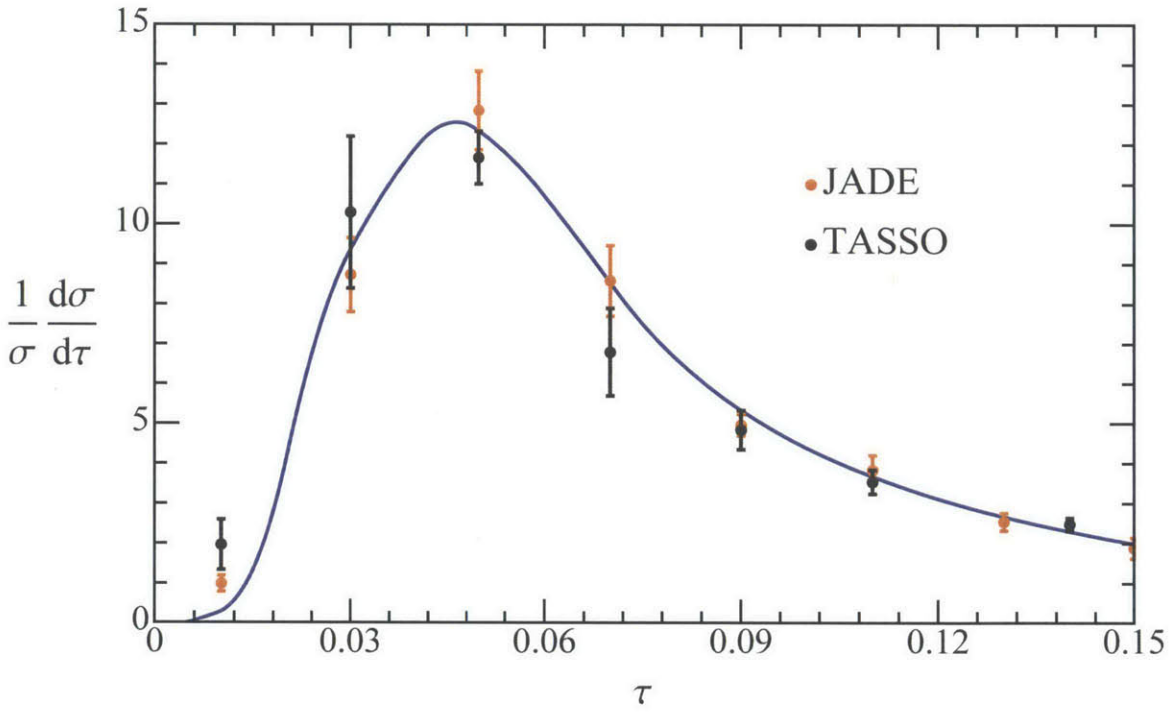

Figure 4-8: Best fit with central profiles at $Q = 44$ GeV. In order to obtain agreement with the first bins at low Q, it is likely that bottom mass effects would have to be included in our analysis.

4.5 Central Profile Fit Results

For our fit with default profile parameters, we obtain $c_1 = 0.131$, $c_2 = 0.244$, $c_3 = 0.141$, and $c_4 = 0.156$ (ensuring $c_0 = 0.938$ for normalization) with experimental uncertainties given by $\sigma_{c_1} = 0.033$, $\sigma_{c_2} = 0.015$, $\sigma_{c_3} = 0.084$, and $\sigma_{c_4} = 0.054$. We also obtain the following correlation matrix:

$$E_c = \begin{pmatrix} 1 & -0.024 & -0.910 & 0.152 \\ -0.024 & 1 & 0.013 & -0.004 \\ -0.910 & 0.013 & 1 & -0.502 \\ 0.152 & -0.004 & -0.502 & 1 \end{pmatrix}, \tag{4.2}$$

where $[E_c]_{ij}$ gives the correlation between c_i and c_j. To compute the uncertainties, we first obtain the covariance matrix by approximating the χ^2 function, with c_0 replaced by $\sqrt{1 - c_1^2 - c_2^2 - c_3^2 - c_4^2}$, as quadratic around the minimum point. The coefficients

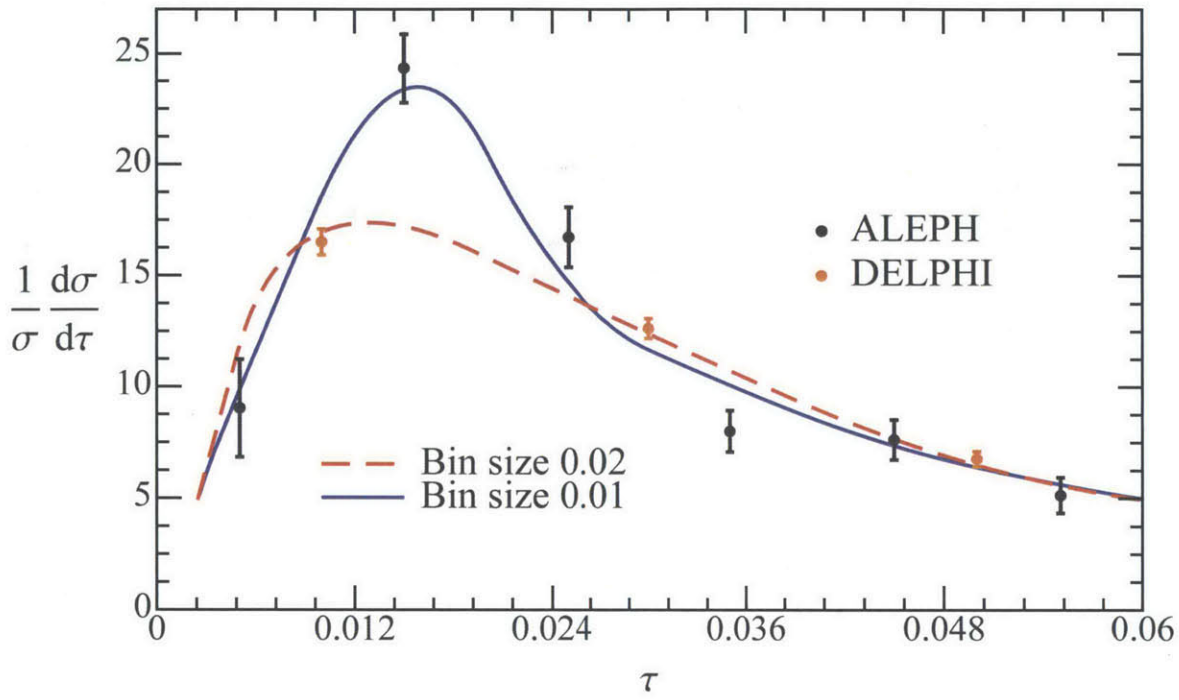

Figure 4-9: Best fit with central profiles at $Q = 200$ GeV. In addition to the consistency of the fit at high Q, this figure illustrates the importance of binning when comparing the predictions of the theory to the data. The apparent disagreement of the blue curve with the DELPHI data is misleading, as the DELPHI data uses wider bins. Integrating over a range corresponding to that of the DELPHI bins demonstrates that our theory agrees with the data, as the red curve illustrates.

of c_i^2 and $c_i c_j$ terms in the approximation are obtained using numerical approximations of the second derivatives at the minimum point. This approximation has the form

$$\chi^2 \simeq \chi^2_{\text{min}} + \sum_{i,j=1}^{4} [M_c^{-1}]_{ij}(c_i - c_i^{\text{best}})(c_j - c_j^{\text{best}}) + \mathcal{O}\left((c_k - c_k^{\text{best}})^3\right), \qquad (4.3)$$

where c_i^{best} are the best-fit values of the c_i and M_c is the covariance matrix. We find this approximation to be in agreement with the true χ^2 function over a range considerably larger than that covered by the 1σ error ellipses, allowing us to treat the experimental uncertainties as Gaussian. We then obtain the elements of the covariance matrix by inverting M_c^{-1}. The square roots of the diagonal elements of M_c give the individual uncertainties σ_{c_i}, and the elements of the correlation matrix E_c are given by

$$[E_c]_{ij} = \frac{[M_c]_{ij}}{\sqrt{[M_c]_{ii}[M_c]_{jj}}}. \tag{4.4}$$

As explained in Chapter 3, the values of the coefficients c_i are basis-dependent and describe the nonperturbative soft function given a particular parameterization. To give a more universal characterization, we report its moments Ω_i corresponding to the best-fit values of the basis coefficients. For the central profiles, we find $\Omega_1 = 0.389 \pm 0.003_{\text{exp}}$ GeV, $\Omega_2 = 0.193 \pm 0.004_{\text{exp}}$ GeV^2, $\Omega_3 = 0.112 \pm 0.004_{\text{exp}}$ GeV^3, and $\Omega_4 = 0.071 \pm 0.004_{\text{exp}}$ GeV^4, where the experimental uncertainties quoted are the square roots of the diagonal elements of the Ω-space covariance matrix. Theory uncertainties are not yet included and are discussed in Section 4.7. We obtain the following correlation matrix:

$$E_\Omega = \begin{pmatrix} 1 & 0.825 & 0.653 & 0.555 \\ 0.825 & 1 & 0.962 & 0.918 \\ 0.653 & 0.962 & 1 & 0.991 \\ 0.555 & 0.918 & 0.991 & 1 \end{pmatrix}. \tag{4.5}$$

The Ω-space covariance matrix is obtained from that of the coefficients c_i through a generalized error propagation formula:

$$\sigma_{\Omega_i,\Omega_j} = \sum_{k=1}^{4}\sum_{\ell=1}^{4} \left(\frac{\partial \Omega_i}{\partial c_k}\right)\left(\frac{\partial \Omega_j}{\partial c_\ell}\right)\sigma_{c_k,c_\ell}. \tag{4.6}$$

The corresponding Ω_i' values can then be computed using Eq. (3.6). We obtain $\Omega_2' = 0.0417 \pm 0.0024_{\text{exp}}$ GeV^2 for the second moment, $\Omega_3' = 0.00445 \pm 0.00073_{\text{exp}}$ GeV^3 for the third, and $\Omega_4' = -0.0017 \pm 0.0038_{\text{exp}}$ GeV^4 for the fourth. No new information is obtained from Ω_1', since it is equivalent to Ω_1. The uncertainties are obtained using the same error propagation method, and we find the correlation matrix

$$E_{\Omega'} = \begin{pmatrix} 1 & 0.322 & -0.021 & -0.476 \\ 0.322 & 1 & 0.695 & -0.934 \\ -0.021 & 0.695 & 1 & -0.778 \\ -0.476 & -0.934 & -0.778 & 1 \end{pmatrix}. \tag{4.7}$$

The relative uncertainties in Ω_i' are greater for higher cumulant moments, as we expect given that the higher moments have a smaller impact on the cross section.

Although we generally plot the cross section at $Q = m_Z$ because of the high precision of the data available at that energy, our fits our global. Figure 4-8 demonstrates the consistency of the central profile fit at the lower value $Q = 44$ GeV. Although the cross section at lower energies is more sensitive to variations in the soft function, this figure illustrates that the cross section is constrained more by the m_Z data than the low Q data due to the large experimental uncertainties at low Q. The fit is consistent at high Q as well, as displayed in Figure 4-9.

4.6 The Shape of the Soft Function

The best-fit soft function presented in Figure 4-4 has multiple peaks, an unphysical feature. This short-scale shaping should not be taken as a claim about the shape of the actual soft function. Rather, the large-scale properties of the function, characterized by its cumulant moments, are consistent with those of the true distribution. To illustrate this point, we construct a more reasonably shaped distribution with similar moments, project it onto our basis, and demonstrate that resulting cross section is similar. We use a beta function given by

$$S_{\text{beta}}(k - 2\bar{\Delta}, \lambda) = \begin{cases} \frac{1}{3.2\lambda} \frac{\Gamma(9.4)}{\Gamma(3.6)\Gamma(5.8)} \left(\frac{k}{3.2\lambda}\right)^{2.6} \left(1 - \frac{k}{3.2\lambda}\right)^{4.8}, & 0 < k < 3.2\lambda \\ 0, & k \leq 0 \text{ or } k \geq 3.2\lambda. \end{cases} \tag{4.8}$$

This beta function has moments (taking into account the proper shifting by $\bar{\Delta}$) given

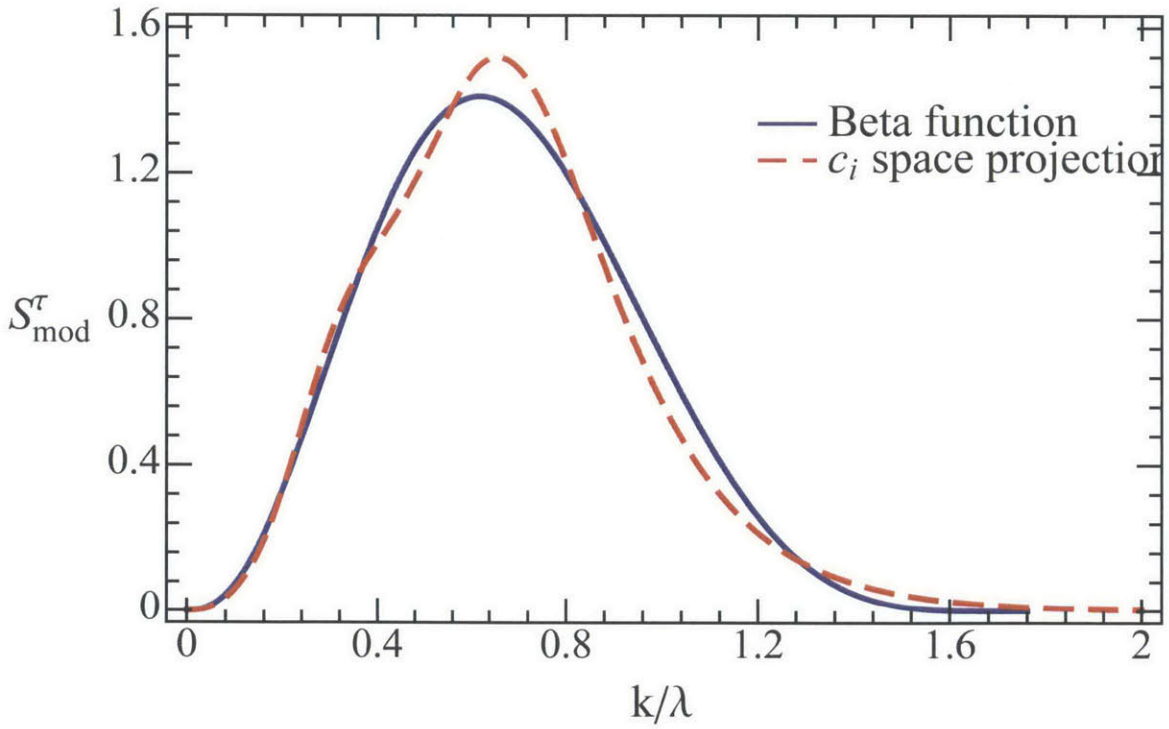

Figure 4-10: The beta function and its projection into c_i space.

by $\Omega_1 = 0.387$ GeV, $\Omega_2 = 0.167$ GeV^2, $\Omega_3 = 0.079$ GeV^3 and $\Omega_4 = 0.040$ GeV^4, which deviate from those of the best fit soft function by 0.5%, -15.5%, -29.5%, and -43.7%, respectively. It is constructed to match the lower moments more closely, since these have the strongest impact on the cross section. Figure 4-10 displays the beta function and its projection onto the basis.

The cross section which results from using S_{beta} is displayed in Figure 4-11, along with the best-fit cross section for comparison. As we expect, at higher τ the cross sections are nearly identical, while at low τ they deviate from each other. In particular, the incorrect higher moments cause the S_{beta} cross section to miss the data in the first bin entirely. The general consistency of the two fits, however, illustrates how a suitable single-peaked distribution with similar moments to those of the best-fit soft function can produce a correct cross section. The physical effects of the soft function are encoded in its moments.

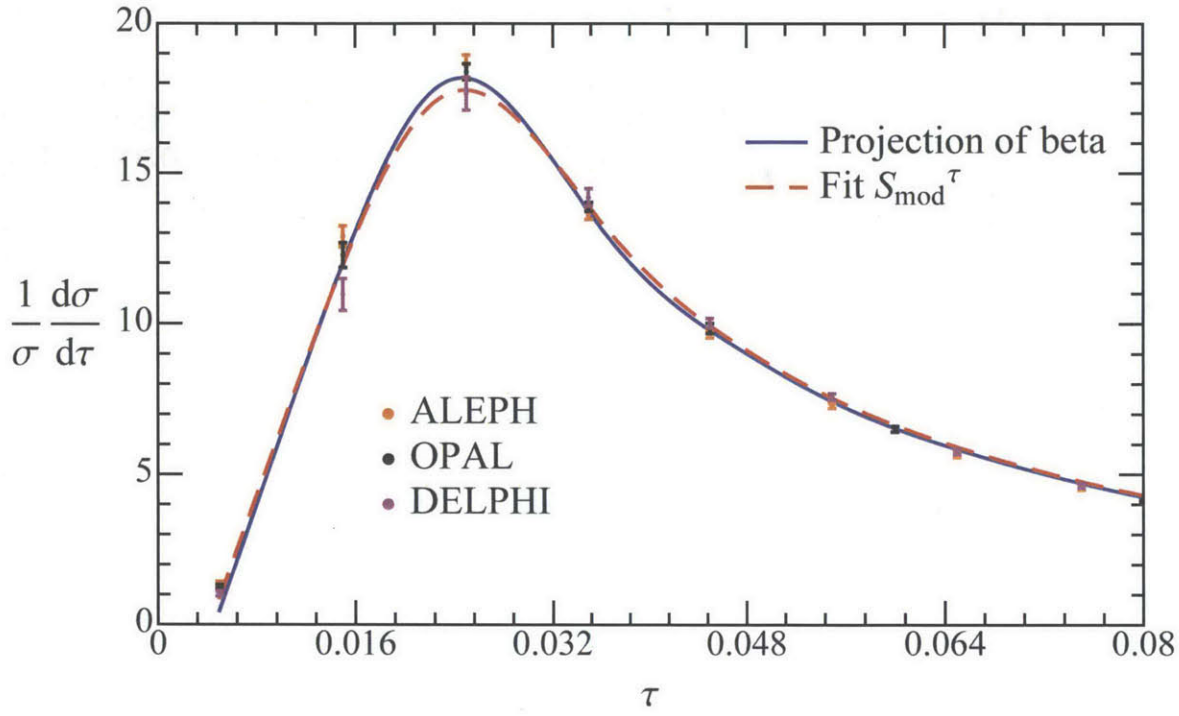

Figure 4-11: A comparison of the best fit soft function with a more reasonable-looking soft function, a beta function projected onto c-space.

4.7 Theory Parameter Scans

Following the approach of [1], we use a random scan to determine the theory uncertainties of the cumulant moments. The parameters we vary in the scans were introduced in Chapter 2; for convenience, their default values and ranges are given in Table 4.1. Our scans contain 500 points, in which each parameter's value is independently chosen from a flat distribution over its range. At each point we use our minimization algorithm to determine fit values for the basis coefficients, from which the cumulant moments are derived.

Unlike [1], in which the best fit value of χ^2 did not change significantly between parameter choices at N^{3}LL$'$, we find that the ability to obtain a reasonable fit in the peak region depends strongly on the choice. As such, we impose a cutoff value for the minimum χ^2 and throw away points with minimum χ^2 above this value. This approach ensures that we do not bias our estimate of the theory uncertainties in Ω_i' with theory choices that do not agree with the data. With the minimum value of

parameter	default value	range
n_0	2.5 GeV	1.5 to 3.5 GeV
n_1	4 GeV	3.5 to 5 GeV
e_H	1	0.5 to 2
e_J	0	$-1, 0, 1$
e_S	0	$-1, 0, 1$
e_R	0	$-1, 0, 1$
n_s	1	$-1, 0, 1$
Γ_3^{cusp}	1553.06	-1553.06 to 4569.18
j_3	0	-3000 to 3000
s_3	0	-500 to 500
ϵ_2	0	$-1, 0, 1$
ϵ_3	0	$-1, 0, 1$

Table 4.1: The parameters varied in our theory scans, along with their values used in our default profile fits. In the first group are parameters associated with the profile functions, in the second are parameters from the singular distribution, and in the third are parameters from the nonsingular distribution.

χ^2 for the central profiles equal to 241.7 with 198 degrees of freedom, we choose 275 as our cutoff for acceptable theories. Figure 4-12 gives the variation of our estimate of the theory uncertainty in Ω_1 as the cutoff value of χ^2 above which points are thrown out increases. The value 275 sits in the first plateau, so we believe that it is a reasonable choice. To numerically estimate central values for the cumulant moments and theory uncertainties, we take the maximum and minimum point kept after imposing the cutoff. We estimate the central values by averaging the maximum and minimum point, and we estimate the theory uncertainty by the half the difference between the maximum and minimum point.

The results of our scans are displayed in Figure 4-13 and Figure 4-14, in which χ^2 cutoffs of 275 and 350 have been respectively applied. We note that unlike for the scan in the tail over (α_s, Ω_1), the space explored by the moments does not shrink at higher orders in perturbation theory. This behavior may be due to the fits being performed at fixed $\alpha_s = 0.1135$ at all orders, or it may be due to the necessity of using different requirements for the choice of cutoff χ^2, which we have not applied.

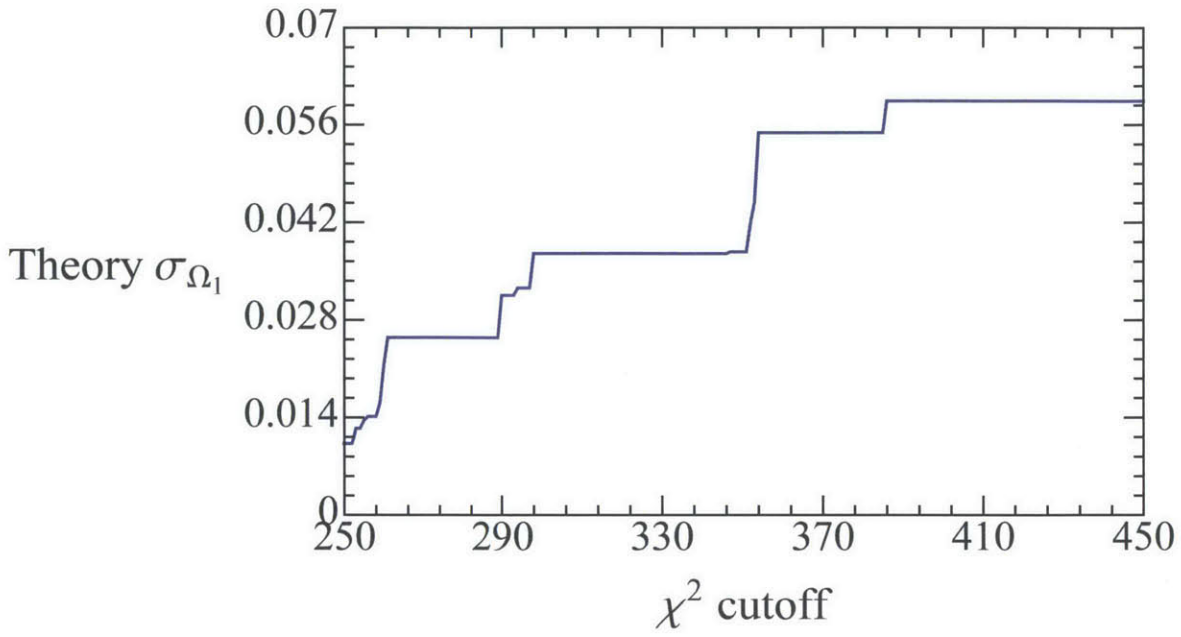

Figure 4-12: The variation in our theory uncertainty estimate of Ω_1 with respect to the imposed χ^2 cutoff. The higher moments exhibit similar behavior.

In a future publication we plan to recompute the scans using variable α_s taken from the best-fit value for the tail at each order. For now we estimate only the theory uncertainties at $\mathrm{N^3LL'}$, where the value of α_s is appropriate.

Using this method and taking the cutoff χ^2 to be 275, we find

$$\begin{aligned}
\Omega_1 &= (0.387 \pm 0.026_{\text{theory}})\text{GeV}, \\
\Omega_2' &= (0.032 \pm 0.011_{\text{theory}})\text{GeV}^2, \\
\Omega_3' &= (3.5 \pm 2.6_{\text{theory}}) \times 10^{-3}\text{GeV}^3, \\
\Omega_4' &= (-0.7 \pm 11.9_{\text{theory}}) \times 10^{-4}\text{GeV}^4.
\end{aligned} \tag{4.9}$$

Experimental uncertainties on the cumulant moments were given in Section 4.5, and we quote the full results in Chapter 5. We note that Ω_1 is determined with considerably more precision by peak fits than by tail fits. The analogous result for Ω_1 given in [1] was 0.323 ± 0.045 GeV, where the 0.045 is the theory uncertainty, which is almost a factor of two larger than the theory uncertainty from the peak fit done here.

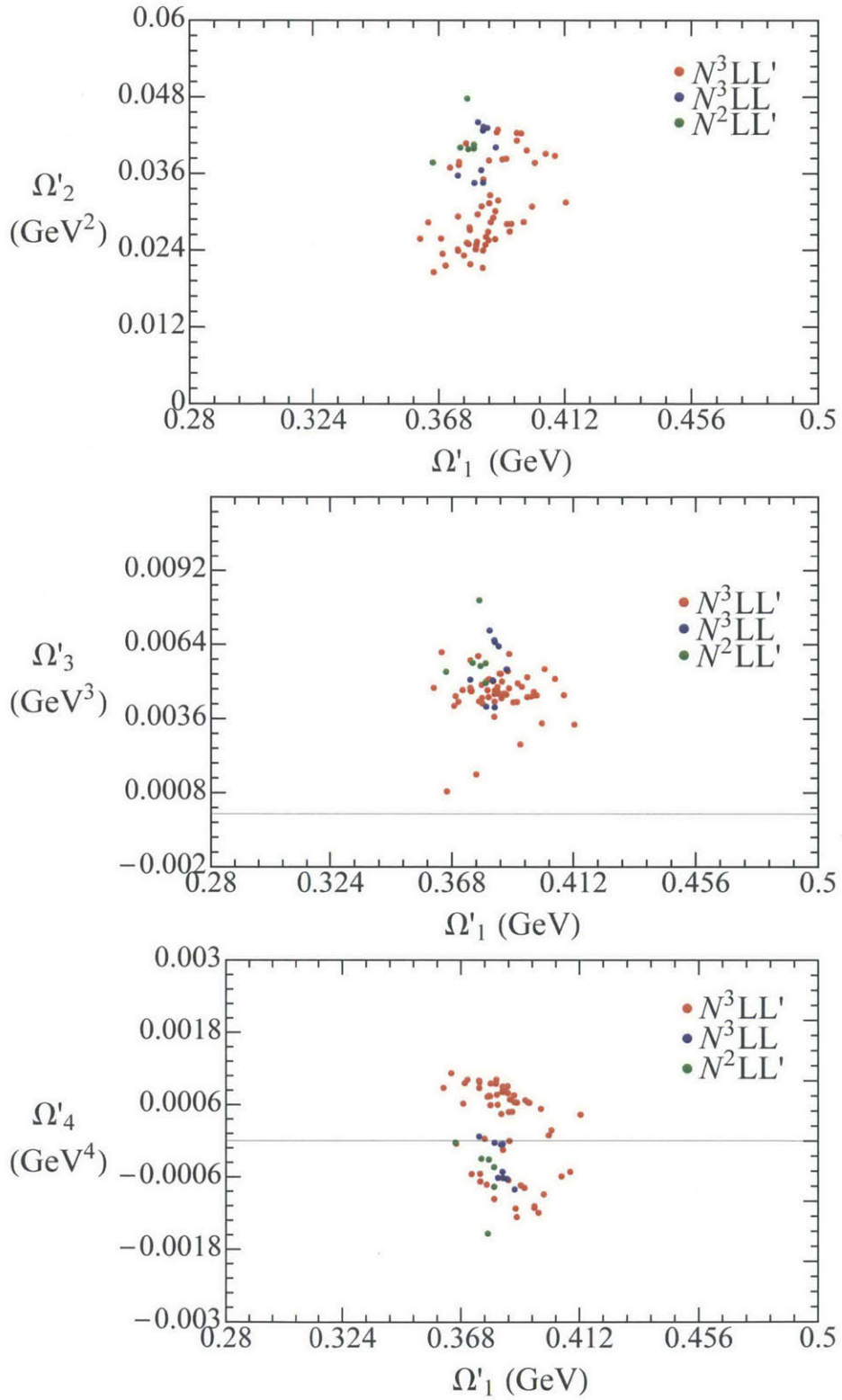

Figure 4-13: Theory scans at N^{3}LL′, N^{3}LL, and N^{2}LL′ are displayed. We neglect correlations between cumulant moments at N^{3}LL′ in our theory uncertainty estimation, since it is clear that they are weak. Here a χ^2 cutoff of 275 has been imposed.

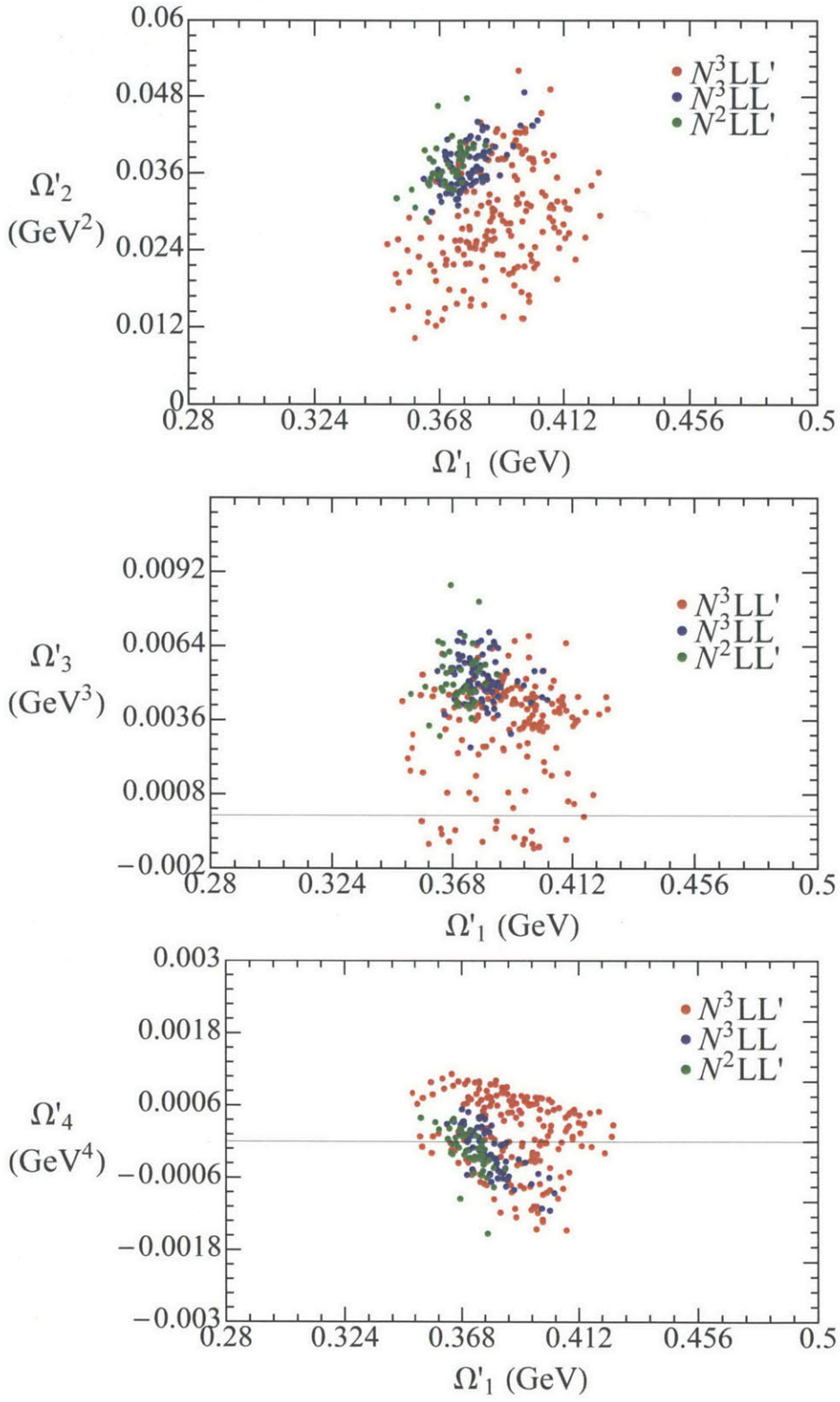

Figure 4-14: For comparison with Figure 4-13, the same scans are displayed here with a χ^2 cutoff of 350 imposed.

Chapter 5

Conclusions

The purpose of this thesis has been to extend the analysis of thrust using SCET by Abbate et al. in Ref. [1] to the peak region of the distribution. We make use of a factorization formula that allows us to split the perturbative components of the distribution into singular and nonsingular terms, governed by energy scales with τ-dependence that we incorporate through the use of profile functions. The factorization formula also contains a nonperturbative soft function, which characterizes uniform soft radiation. The effects of the soft function are particularly pronounced in the peak region, and so fits to the experimental data there provide an excellent method of determining its properties. We write the soft function as an infinite sum of basis functions with coefficients c_i, and it is these coefficients which we fit to the data in our χ^2 minimization procedure. We then use these coefficients and their uncertainties to determine the cumulant moments Ω_i', which describe the physical properties of the soft function independently of a particular parameterization.

We have demonstrated that including more basis functions in our fit for the soft function improves the agreement with the experimental data substantially, with the minimum reduced χ^2 from our central profiles fit at N^{3}LL$'$ decreasing from 5.29 without fitting basis functions (and setting $c_0 = 1$) to 1.23 with the first five basis functions included. We have also computed best-fit values for the Ω_i' from $i = 1$ to 4 and computed experimental and theoretical uncertainties and experimental correlations for our central profiles at N^{3}LL' for each. To determine the perturbative uncertainties,

we use a scan procedure, taking 500 random choices of the undetermined parameters of the theory and performing fits to determine the Ω_i' for each. For our final results we find

$$\begin{aligned}
\Omega_1 &= (0.387 \pm 0.003_{\text{exp}} \pm 0.026_{\text{theory}})\ \text{GeV}, \\
\Omega_2' &= (0.032 \pm 0.002_{\text{exp}} \pm 0.011_{\text{theory}})\ \text{GeV}^2, \\
\Omega_3' &= (3.5 \pm 0.7_{\text{exp}} \pm 2.6_{\text{theory}}) \times 10^{-3}\ \text{GeV}^3, \\
\Omega_4' &= (-0.7 \pm 3.8_{\text{exp}} \pm 11.9_{\text{theory}}) \times 10^{-4}\ \text{GeV}^4.
\end{aligned} \tag{5.1}$$

We have obtained the most accurate characterization of the peak region for thrust available at this time. This work will contribute to a future publication. There we plan to address the impact of theory uncertainty at different perturbative orders in greater detail.

Bibliography

[1] R. Abbate, M. Fickinger, A. H. Hoang, V. Mateu, and I. W. Stewart, Phys. Rev. D83, 074021 (2011), 1006.3080.

[2] A. H. Hoang and I. W. Stewart, Phys. Lett. B660, 483 (2008), 0709.3519.

[3] R. K. Ellis, W. J. Stirling, and B. R. Webber, QCD and Collider Physics, Cambirdge Monographs on Particle Physics, Nuclear Physics, and Cosmology, Cambridge University Press (1996).

[4] S. Kluth, Rept. Prog. Phys. 69, 1771 (2006), hep-ex/0603011.

[5] R. K. Ellis, D. A. Ross, and A. E. Terrano, Nucl. Phys. B178, 421 (1981).

[6] S. Catani and M. H. Seymour, Phys. Lett. B378, 287 (1996), hep-ph/9602277.

[7] S. Catani and M. H. Seymour, Nucl. Phys. B485, 291 (1997), hep-ph/9605323.

[8] A. Gehrmann-De Ridder, T. Gehrmann, E. W. N. Glover, and G. Heinrich, Phys. Rev. Lett. 99, 132002 (2007), 0707.1285.

[9] Z. Ligeti, I. W. Stewart, and F. J. Tackmann, Phys. Rev. D78, 114014 (2008), 0807.1926.

[10] W. Braunschweig et al. (TASSO), Z. Phys. C47, 187 (1990).

[11] Y. K. Li et al. (AMY), Phys. Rev. D41, 2675 (1990).

[12] P. A. Movilla Fernandez, O. Biebel, S. Bethke, S. Kluth, and P. Pfeifenschneider (JADE), Eur. Phys. J. C1, 461 (1998), hep-ex/9708034.

[13] K. Abe et al. (SLD), Phys. Rev. D51, 962 (1995), hep-ex/9501003.

[14] B. Adeva et al. (L3), Z. Phys. C55, 39 (1992).

[15] P. Achard et al. (L3), Phys. Rept. 399, 71 (2004), hep-ex/0406049.

[16] J. Abdallah et al. (DELPHI), Eur. Phys. J. C29, 285 (2003), hep-ex/0307048.

[17] P. Abreu et al. (DELPHI), Eur. Phys. J. C14, 557 (2000), hep-ex/0002026.

[18] D. Wicke (1999), wU-B-DIS-1999-05.

[19] P. Abreu et al. (DELPHI), Phys. Lett. B456, 322 (1999).

[20] G. Abbiendi et al. (OPAL), Eur. Phys. J. C40, 287 (2005), hep-ex/0503051.

[21] K. Ackerstaff et al. (OPAL), Z. Phys. C75, 193 (1997).

[22] G. Abbiendi et al. (OPAL), Eur. Phys. J. C16, 185 (2000), hep-ex/0002012.

[23] A. Heister et al. (ALEPH), Eur. Phys. J. C35, 457 (2004).

[24] A. Gehrmann-De Ridder, T. Gehrmann, E. W. N. Glover, and G. Heinrich, Phys. Rev. Lett. 99, 132002 (2007), 0707.1285.

[25] A. Gehrmann-De Ridder, T. Gehrmann, E. W. N. Glover, and G. Heinrich, JHEP 12, 094 (2007), 0711.4711.

[26] S. Weinzierl, Phys. Rev. Lett. 101, 162001 (2008), 0807.3241.

[27] S. Weinzierl, JHEP 06, 041 (2009), 0904.1077.

[28] C. W. Bauer, S. Fleming, and M. E. Luke, Phys. Rev. D 63, 014006 (2001), hep-ph/0005275.

[29] C. W. Bauer, S. Fleming, D. Pirjol, and I. W. Stewart, Phys. Rev. D 63, 114020 (2001), hep-ph/0011336.

[30] C. W. Bauer and I. W. Stewart, Phys. Lett. B 516, 134 (2001), hep-ph/0107001.

[31] C. W. Bauer, D. Pirjol, and I. W. Stewart, Phys. Rev. D65, 054022 (2002), hep-ph/0109045.

[32] C. W. Bauer, S. Fleming, D. Pirjol, I. Z. Rothstein, and I. W. Stewart, Phys. Rev. D 66, 014017 (2002), hep-ph/0202088.

[33] C. W. Bauer, A. V. Manohar, and M. B. Wise, Phys. Rev. Lett. 91, 122001 (2003), hep-ph/0212255.

[34] C. W. Bauer, C. Lee, A. V. Manohar, and M. B. Wise, Phys. Rev. D 70, 034014 (2004), hep-ph/0309278.

[35] S. Fleming, A. H. Hoang, S. Mantry, and I. W. Stewart, Phys. Rev. D77, 074010 (2008), hep-ph/0703207.

[36] M. D. Schwartz, Phys. Rev. D77, 014026 (2008), 0709.2709.

[37] A. H. Hoang and I. W. Stewart, Phys. Lett. B660, 483 (2008), 0709.3519.

[38] G. P. Korchemsky (1998), hep-ph/9806537.

[39] G. P. Korchemsky and G. Sterman, Nucl. Phys. B555, 335 (1999), hep-ph/9902341.

[40] G. P. Korchemsky and S. Tafat, JHEP 10, 010 (2000), hep-ph/0007005.